Iron valence systematics in clinopyroxene crystals from ocean island basalts

David A. Neave[1*], Alexander G. Stewart[1], Margaret E. Hartley[1], Olivier Namur[2]

[1*]Department of Earth and Environmental Sciences, The University of Manchester, Manchester, M13 9PL, United Kingdom.
[2]Department of Earth and Environmental Sciences, KU Leuven, BE-3001 Leuven, Belgium.

*Corresponding author(s). E-mail(s): david.neave@manchester.ac.uk;

Abstract

The valence state of Fe plays a vital role in setting and recording the oxidation state of magmas, commonly expressed in terms of oxygen fugacity ($\boldsymbol{f_{O_2}}$). However, our understanding of the nature and causes of $\boldsymbol{f_{O_2}}$ variability within and between magmatic systems remains patchy because of the challenges associated with estimating Fe valence in glasses and minerals robustly and routinely. Here we present analyses of clinopyroxene crystals from OIB samples erupted in Iceland and the Azores performed to investigate their Fe valence systematics and explore their potential for recording information about magma Fe^{3+} contents and $\boldsymbol{f_{O_2}}$ conditions. Although many studies assume that all Fe in magmatic clinopyroxene crystals occurs as Fe^{2+}, we find that up to half of the total Fe present in magmatic clinopyroxene crystals may occur as Fe^{3+}, with crystals from alkali systems typically containing more Fe^{3+} than those from tholeiitic systems. Thus, Fe^{3+} is a major if under-appreciated constituent of clinopyroxene crystals erupted from ocean island volcanoes. Most Fe^{3+} in these crystals is hosted within esseneite component ($CaFe^{3+}AlSiO_6$), though some can be hosted in aegirine component ($NaFe^{3+}Si_2O_6$) in crystals from alkali systems. Observations from samples containing quenched matrix glasses suggest that the incorporation of Fe^{3+} is mediated by the abundance of tetrahedrally coordinated Al (^{IV}Al), implying strong steric controls over Fe^{3+} partitioning between clinopyroxene and liquid (i.e., $\boldsymbol{D^{cpx-liq}_{Fe_2O_3}}$ values). For example, ^{IV}Al-rich prism sectors of sector-zoned crystals contain more Fe^{3+} than hourglass sectors. Moreover, ^{IV}Al-rich compositions formed during disequilibrium crystallisation at high degrees of undercooling are also enriched in Fe^{3+}. Apparent clinopyroxene-liquid

Fe^{2+}–Mg exchange equilibria (i.e., $\boldsymbol{K^{cpx-liq}_{D,Fe^{2+}-Mg}}$ values) are similarly affected by disequilibrium crystallisation. Nonetheless, it is possible to reconcile our observed clinopyroxene compositions with glass Fe valence systematics estimated from olivine-liquid equilibria if we assume that equilibrium was best recorded by the lowest-Fe^{3+} compositions in clinopyroxene crystals affected by disequilibrium crystallisation. In this case, olivine-liquid and clinopyroxene-liquid equilibria record equivalent narratives, with our glassy samples from Iceland recording evolution under $\boldsymbol{f_{O_2}}$ conditions about one log unit above fayalite-magnetite-quartz (FMQ) equilibrium (i.e., ∼FMQ+1) and our glassy Azorean sample recording evolution under significantly more oxidising conditions (∼FMQ+2.5) before experiencing syn-eruptive reduction, likely as a result of $\boldsymbol{SO_2}$ degassing. Overall, our findings demonstrate that the Fe valence systematics of clinopyroxene crystals record important information about the conditions under which OIBs evolve, but that further experimental work is required to properly disentangle the effects of magma composition, disequilibrium and $\boldsymbol{f_{O_2}}$ conditions on clinopyroxene-liquid equilibria involving Fe^{2+} and Fe^{3+}.

Keywords: clinopyroxene, ferric iron, ocean island basalt, iron valence, partitioning

Introduction

Magmas erupted in different tectonic settings often record evolution under different oxygen fugacity (f_{O_2}) conditions (Wood et al, 1990; Carmichael, 1991; Cottrell et al, 2022), where f_{O_2} reflects the chemical potential of O in a magma. These different f_{O_2} conditions ultimately reflect differences in the pressure-temperature-composition (PTX) conditions under which magmas evolve in different tectonic settings. In particular, the valence state of Fe plays a central role in setting magmatic f_{O_2} because Fe is by far the most abundant multivalent element in terrestrial magmas (Frost, 1991). Specifically, the greater the ratio of ferric-to-total Fe ($Fe^{3+}/\Sigma Fe$, where $\Sigma Fe = Fe^{2+} + Fe^{3+}$) in a magma of any given composition, the greater its f_{O_2}, as described by various $(P)TX$-dependent parametrisations (Kress and Carmichael, 1991; Berry et al, 2018; Borisov et al, 2018). Moreover, understanding coupled variations in the f_{O_2} and $Fe^{3+}/\Sigma Fe$ content of magmas is is important because of the first-order control they exert over magmatic phase equilibria (e.g., Toplis and Carroll, 1995; Feig et al, 2010), volatile solubilities (e.g., Jugo, 2009; O'Neill, 2021; Hughes et al, 2023) and equilibrium vapour compositions (e.g., Burgisser and Scaillet, 2007; Oppenheimer et al, 2011). Magma $Fe^{3+}/\Sigma Fe$ contents thus determine the trajectories along which magmas evolve, the nature of the solids they crystallise, and the abundance and speciation of the volatiles they release, which in turn control ore formation processes and mediate long-term planetary habitability (Holland, 2002; Evans and Tomkins, 2011; Gaillard et al, 2011). Generating internally consistent datasets of magma $Fe^{3+}/\Sigma Fe$ contents is thus a vital step towards improving our understanding of Earth's evolution and behaviour over geological time. We aim to further this endeavour by studying the valence state of iron in clinopyroxene crystals, a significant but poorly understood host of Fe^{3+} in magmatic systems.

It is generally, though not universally (cf., Lee et al, 2005, 2012), accepted that arc basalts have higher $Fe^{3+}/\Sigma Fe$ contents and evolve under more oxidising conditions (approximately one log unit above fayalite-magnetite-quartz equilibrium; ~FMQ+1) than mid-ocean ridge basalts (MORBs; close to FMQ), even if the reasons for this remain contested (Evans, 2006; Kelley and Cottrell, 2009; Gaetani, 2016; Brounce et al, 2019; Cottrell et al, 2022; Evans and Tomkins, 2022). Many ocean island basalts (OIBs) also appear to have evolved under more oxidising conditions than MORBs, though global differences between MORBs and OIBs are decidedly more ambiguous than those between MORBs and arc basalts. Observations from Lanzarote and El Hierro in the Canary Islands, Fogo in Cape Verde and Erebus in Antarctica suggest that some OIBs evolve at ~FMQ+2 or higher depending on the oxybarometer used (Moussallam et al, 2014, 2019; Taracsak et al, 2022; Nicklas et al, 2022b). Observations from Laki in Iceland and Kīlaeua and Mauna Kea in Hawaii also imply evolution under somewhat elevated f_{O_2} conditions that extend up to ~FMQ+1 (Moussallam et al, 2016; Hartley et al, 2017; Helz et al, 2017; Brounce et al, 2017). In contrast, OIBs from Piton de la Fournaise on Réunion appear to have evolved under comparable f_{O_2} conditions to MORBs at or even below FMQ (Brounce et al, 2022; Nicklas et al, 2022a). While Réunion's divergence from other OIBs may appear challenging to reconcile, Brounce et al (2022) propose an explanation based on known geochemical differences between ocean island systems. Specifically, they suggest that relatively oxidised OIBs are derived from mantle sources rich in recycled components and thus Fe^{3+} (EMI, EMII and HIMU), while relatively reduced OIBs are derived from mantle sources poor in recycled components and Fe^{3+}(C/FOZO/PREMA; Zindler and Hart, 1986; Stracke, 2012; Weis et al, 2023). Nevertheless, internally consistent estimates of magmatic f_{O_2} conditions or magma $Fe^{3+}/\Sigma Fe$ contents across different ocean island volcanoes needed to verify or refute this proposition remain scarce. We aim to address this by investigating the valence state of Fe in volcanic glasses and clinopyroxene crystals from Iceland and the Azores that erupt samples with affinities towards C/FOZO/PREMA and EMII reservoirs, respectively.

Considerable progress has been made in using glass and mineral compositions to estimate magmatic f_{O_2} conditions over recent decades, with two-oxide oxybarometry and Fe-XANES spectroscopy of volcanic glasses being especially fruitful (Cottrell et al, 2022, and references therein). However, the former depends on the presence of magnetite and ilmenite pairs that have remained in equilibrium since their formation (e.g., Bacon and Druitt, 1988; Ghiorso and Evans, 2008), and the latter on the presence of pristine volcanic glass and access to a synchrotron radiation source (e.g., Cottrell et al, 2009; Muth and Cottrell, 2023). Furthermore, the reduction of magmatic liquids by SO_2 degassing during magma ascent and sensitivity of hydrous glasses to beam damage add further complexity to interpreting results from Fe-XANES spectroscopy (Moussallam et al, 2016; Brounce et al, 2017; Cottrell et al, 2018). Glass and mineral $Fe^{3+}/\Sigma Fe$ contents can also be determined by Mössbauer spectroscopy (e.g., McCammon, 2021). However, laboratory-based Mössbauer spectroscopy is ill suited to high analytical throughput and synchrotron-based Mössbauer spectroscopy can only be performed a limited number of facilities, limiting the overall utility of the approach. Fortunately, different f_{O_2}-sensitive mineral-mineral or mineral-liquid equilibria can

allow us to circumvent these issues and recover better estimates of magmatic f_{O_2}, especially if the time taken for minerals to respond to syn- or post-eruptive changes in f_{O_2} is longer than for magmatic liquids. Recent re-evaluations of olivine-liquid equilibria that have explicitly addressed challenges in parametrising Fe^{2+}–Mg exchange (i.e., predicting $K^{ol-liq}_{D,Fe^{2+}-Mg}$) in systems with variable glass $Fe^{3+}/\Sigma Fe$ contents provide a potential avenue for oxybarometry without access to Fe-XANES spectroscopy (Blundy et al, 2020; Davis and Cottrell, 2021; Saper et al, 2022). While developing similar tools based on clinopyroxene-liquid equilibria is complicated by steric effects associated with crystal structure of clinopyroxene, we aim to exploit comparatively well understood olivine-liquid equilibria to gain new insights into Fe^{3+} partitioning and Fe^{2+}–Mg exchange between clinopyroxene crystals and their host melts. A key goal of this work is to start building a better understanding how clinopyroxene compositions reflect magmatic f_{O_2} conditions.

Magmatic clinopyroxene crystals incorporate both Fe^{2+} and Fe^{3+} by virtue of hosting three distinct cation sites: clinopyroxene has the general formula $M2(R^{2+})M1(R^{2+})T_2(2R^{4+})O_6$, where R is a metal cation, M2 is a distorted octahedral site, M1 is a regular octahedral site and T is a tetrahedral site typically occupied by Si forming the Si_2O_6 chains that define the pyroxene structure (Morimoto et al, 1988). As a consequence, clinopyroxene crystals should be inherently sensitive to magmatic $Fe^{3+}/\Sigma Fe$ contents and f_{O_2} conditions. However, little is known about Fe valence systematics in magmatic clinopyroxene crystals, which fundamentally limits our ability to explore relationships between f_{O_2} and clinopyroxene compositions. This in turn restricts our capacity to describe phase equilibria relations in natural and experimental systems, as well as calibrate the thermodynamic datasets that underpin algorithms like MELTS, THERMOCALC and MAGEMin that are widely used to model magmatic processes (Sack and Ghiorso, 1994; Ghiorso and Sack, 1995; Holland and Powell, 1998; Powell et al, 1998; Jennings and Holland, 2015; Holland et al, 2018; Riel et al, 2022). Experiments performed on a Martian (i.e., shergottites-nahklites-chassignites (SNC)-group) meteorite composition under relatively reducing conditions (∼FMQ−4.7 to ∼FMQ+0.3) suggest that f_{O_2} correlates with clinopyroxene $Fe^{3+}/\Sigma Fe$, though this inference is based on highly uncertain clinopyroxene $Fe^{3+}/\Sigma Fe$ determinations (McCanta et al, 2004). However, it is possible that the reducing conditions under which these experiments were performed and the poor precision of unoriented Fe-XANES spectroscopy performed on experimentally produced clinopyroxene crystals masked the true nature of relationships between f_{O_2} and clinopyroxene $Fe^{3+}/\Sigma Fe$. Indeed, we speculate that our poor understanding of clinopyroxene $Fe^{3+}/\Sigma Fe$ contents in magmatic systems more generally reflects the challenges associated with determining Fe valence in mineral samples, whether by bulk methods or *in situ* microanalysis requiring access to a Mössbauer spectrometer or synchrotron radiation source (Canil and O'Neill, 1996; Dyar et al, 2002; McCammon, 2021; Steven et al, 2022).

Neave et al (2024) recently re-evaluated previously discredited approaches for estimating clinopyroxene Fe^{3+} contents from stoichiometric constraints (cf., McGuire et al, 1989; Canil and O'Neill, 1996). By optimising the electron probe microanalysis (EPMA) technique used to measure clinopyroxene, they demonstrated that clinopyroxene $Fe^{3+}/\Sigma Fe$ contents can be accurately determined by stoichiometry using the

approach of Droop (1987) to precision similar to that achievable with Mössbauer spectroscopy. They also demonstrated that more than half of the Fe present in natural augite crystals can occur as Fe^{3+}, in line with sparse analyses of augite crystals from mafic alkaline rocks by Mössbauer spectroscopy that are available in the literature (McGuire et al, 1989; Weis et al, 2015). They also proposed a new scheme for assigning clinopyroxene components that explicitly accounts for the presence of Fe^{3+}. Specifically, they assigned most Fe^{3+} to esseneite component (Es, $CaFe^{3+}AlSiO_6$) via a Tschermak-type substitution, with some Fe^{3+} potentially being assigned to aegirine component (Ae, $NaFe^{3+}Si_2O_6$) formed from any Na remaining after forming jadeite component (Jd, $NaAlSi_2O_6$). Here we seek to provide the first systematic survey of Fe valence and Fe^{3+}-sensitive clinopyroxene componentry in diverse OIB samples. Only by developing this deeper understanding of clinopyroxene $Fe^{3+}/\Sigma Fe$ systematics will it eventually become possible to investigate how clinopyroxene compositions and phase equilibria involving clinopyroxene reflect magma $Fe^{3+}/\Sigma Fe$ contents and ultimately f_{O_2} conditions.

Here we present high-precision analyses of clinopyroxene crystals in OIB samples from Iceland and the Azores in which clinopyroxene $Fe^{3+}/\Sigma Fe$ contents have been estimated by stoichiomery following the approach of Droop (1987). By applying the revised scheme for assigning clinopyroxene components proposed by Neave et al (2024), we show how Fe^{3+} is an important constituent of clinopyroxene crystals from diverse natural magmas that cannot readily be ignored in our treatment of clinopyroxene compositions. Finally, we use our improved understanding of magmatic clinopyroxene $Fe^{3+}/\Sigma Fe$ contents to explore Fe^{3+} partitioning and Fe^{2+}–Mg exchange equilibria between clinopyroxene crystals and basaltic melts in OIB samples that evolved under different f_{O_2} conditions.

Samples

We studied six OIB samples erupted from well-characterised but geochemically distinct magmatic systems in the North Atlantic (Figure 1). We investigated samples ranging from tholeiitic and alkali basalts to ankaramites and tephites in order to evaluate major element controls on clinopyroxene compositions and the effects of anticipated variations in magmatic f_{O_2} conditions on clinopyroxene $Fe^{3+}/\Sigma Fe$ contents (Moussallam et al, 2019; Cottrell et al, 2022). Lava samples were cut into polished thin sections and tephra samples were mounted in epoxy prior to imaging and microanalysis.

Tholeiitic and moderately primitive (∼7 wt.% MgO) pillow basalt samples (HOR-11-01 and SKU-11-18) were collected from Skuggafjöll mountain in the Eastern Volcanic Zone (EVZ) of southern Iceland. The petrology of these samples and Skuggafjöll more generally is described by Neave et al (2014). A tholeiititc and moderately primitive (∼7 wt.% MgO) basaltic tephra sample was collected from 2014–2015 Holuhraun eruption in the Northern Volcanic Zone (NVZ) of central Iceland. Our sample is equivalent to sample H14 described by Halldórsson et al (2018), who also described the petrological evolution of the wider eruption. A tholeiitic and moderately evolved (∼4.5 wt.% MgO) basaltic lava sample (LAK-04) was collected from the Laki

lava flow in the EVZ southern Iceland. The petrology of LAK-04 and the Laki lava flow as a whole is described by Passmore et al (2012) and Neave et al (2013).

Three ankaramite (highly olivine- and clinopyroxene-phyric alkali basalts) lava samples (HVAM13-01, ARN13-01 and HLTS13-01, from Hvammsmúli, Arnarholl and Holtsdalur, respectively) were collected from Eyjafjalljökull in the the EVZ of southern Iceland. The petrology of some of these ankaramite localities is described by Loughlin (1995) and Nikkola et al (2019). An alkali basalt lava sample (PI-011) was collected from the northern flank of Pico volcano in the Azores while a trachybasaltic-to-tephritic tephra sample (PI-041) was collected from a vent on the Panalto da Achada fissure system on the southeastern flank. The petrology of Pico is discussed in detail by Fran ca et al (2006), Zanon et al (2020) and van Gerve et al (2024).

Methods

In preparation for EPMA, backscattered electron (BSE) images were collected from epoxy mounts and thin sections using a FEI Quanta 650F scanning electron microscope (SEM) in the Department of Earth and Environmental Sciences at the University of Manchester. Imaging was performed to characterise compositional variability within and between our samples, with a particular focus on clinopyroxene crystals often characterised by complex sector and concentric zoning (e.g., Leung, 1974; Dowty, 1976; Ubide et al, 2019; Neave et al, 2019).

Quantitative analyses of clinopyroxene, olivine, plagioclase, oxides and glass were performed by EPMA using a JEOL JXA8530F instrument in the School of Earth Sciences at the University of Bristol operated with Probe for EPMA (https://www.probesoftware.com/). The following primary standards were used for calibration: Si, albite; Ti, TiO_2; Al, sanidine; Cr, Cr_2O_3; Fe, hematite; Mn, Mn metal; Mg, St. John's olivine; Ca, wollastonite; Na, albite; K, sanidine; P, Durango apatite; and Ni, Ni metal.

Different analytical conditions were used for different phases, with particular care taken over clinopyroxene analyses to ensure that $Fe^{3+}/\Sigma Fe$ could be determined by stoichiometry (Neave et al, 2024). We used an accelerating voltage of 15 kV and a spot size of 1 μm to analyse clinopyroxene, olivine and oxides. The following elements were analysed with a current of 10 nA (on-peak counting times in seconds are shown in parentheses; background counting times were half on-peak counting times): Si(20), Ti(20), Al(20), Fe(40), Mg(40), Ca(20) and K(40); and the following elements were analysed with a current of 40 nA: Cr(60), Mn(30), Na(60), P(60) and Ni(30). We used this approach to maximise the precision of minor element analyses in clinopyroxene that affect the precision of stoichiometric determinations of $Fe^{3+}/\Sigma Fe$ (Neave et al, 2024). All elements in plagioclase and glass were analysed with an accelerating voltage of 15 kV, a defocused 10 μm spot and a current of 10 nA (on-peak counting times in seconds are shown in parentheses; background counting times were half on-peak counting times): Si(10), Ti(50), Al(10), Cr(10), Fe(30), Mn(30), Mg(50), Ca(10), Na(10), K(10) and P(40).

Accuracy was monitored by analysing the following secondary standards: in-house diopside, Cr-diopside and labradorite, and international kk1 kaersutite (Reay et al,

1989), BCR-2G basaltic glass (Jochum et al, 2005). Major element (e.g., SiO_2 and MgO in glass and clinopyroxene) concentrations were typically within 2% of preferred values (based on published values for international standards or longitudinal data for in-house standards), while minor element (e.g., Cr_2O_3 and Na_2O in Cr-diopside and FeO_T in plagioclase) concentrations were typically within 6% of preferred values. Counting statistics from analyses of unknown clinopyroxene crystals indicate that major (SiO_2, Al_2O_3, FeO_T, MgO and CaO) and minor (TiO_2, Cr_2O_3 and Na_2O) elements were determined with 1σ precisions better than 1% and 5%, respectively; only MnO was measured with a worse 1σ precision of ∼8%. Olivine, plagioclase, oxides and glass were measured with comparable 1σ precisions: better than 2% for major elements and better than 5% for most minor elements. Full details of secondary standard analyses and analytical precision are provided alongside all EPMA data in the Supplementary Material.

Results

Petrography

Tholeiitic pillow basalt samples HOR-11-01 and SKU-11-18 from Skuggafjöll contain macrocrysts of plagioclase, clinopyroxene and olivine in a glassy to microcrytalline and somewhat vesicular groundmass (Neave et al, 2014). Macrocrysts are defined as being >100 μm in length and texturally distinct from the groundmass (e.g., Thomson and Maclennan, 2013). Clinopyroxene macrocrysts are up to ∼500 μm in length and often occur in ophitic arrangement with plagioclase. They typically show weak oscillatory zoning and prominent hourglass sector zoning with low-BSE-intensity $\{\bar{1}11\}$ hourglass sectors and high-BSE-intensity $\{hk0\}$ prism sectors (Figure 2A; Neave et al, 2019).

The tholeiitic basalt tephra sample from Holuhraun contains macrocrysts of plagioclase, clinopyroxene and olivine in a glassy and highly vesicular groundmass (Halldórsson et al, 2018). Clinopyroxene macrocrysts are up to ∼250 μm in length and often occur in ophitic arrangement with plagioclase, and also sometimes in association with olivine. Most show weak oscillatory and hourglass sector zoning, though this is not well resolved at the resolution of our BSE images (Figure 2B).

The tholeiitic basalt lava sample LAK04 from Laki contains macrocrysts of plagioclase, clinopyroxene and olivine in a microcrystalline and vesicular groundmass (Passmore et al, 2012; Neave et al, 2013). Clinopyroxene macrocrysts up to ∼800 μm occur in ophitic arrangement with plagioclase, most often in multiphase glomerocrysts that also contain olivine (Figure 2C). Most clinopyroxne crystals also show concentric and hourglass sector zoning like that observed in our samples from Skuggafjöll.

Ankaramitic lava samples HVAM13-01, ARN13-01 and HLTS13-01 from Eyjafjallajökull are dominated by large macrocrysts of olivine and clinopryoxene and smaller oxide macrocrysts in microcrystalline groundmasses, though some plagioclase macrocrysts occur in ARN13-01. Clinopyroxene macrocrysts up to ∼5 mm in length typically occur as individual, euhedral to subhedral crystals, with some occurring in association with olivine (Figure 2D). Most clinopryoxene crystals are characterised by concentric core-to-rim zoning, though crystals in HVAM13-01 appear to show reaction rims consistent with dissolution prior to final solidification (Neave and Maclennan, 2020).

The alkali basalt lava PI-011 from Pico contains large macrocrysts of clinopyroxene, olivine, plagioclase, magnetite and ilmenite in a microcrystalline and vesicular groundmass that also contains microcrysts (crystals <100 μm in length that are distinct from the groundmass) of the same phases. Clinopyroxene macrocrysts up to ∼4 mm in length generally occur as individual, euhedral crystals, though some occur in glomerocrysts with olivine and/or plagioclase. Most crystals show slight core-to-rim zoning imprinted on complex patchy sector zoning (Figure 2E).

The trachybasaltic-to-tephritic tephra sample PI-041 from Pico contains macrocrysts of clinopyroxene, olivine, plagioclase, magnetite and ilmenite in a glassy and highly vesicular groundmass that also contains microcrysts of the same phases. Clinopyroxene macrocrysts up to ∼2 mm in length generally occur as individual, euhedral to subhedral crystals, though some occur in association with olivine and ilmenite. Clinopyroxene crystals show evidence for both core-to-rim zoning and complex patchy sector zoning (Figure 2F).

Major element chemistry

The major element chemistry of clinopyroxene crystals in our OIB samples is summarised in a series of pyroxene quadrilateral diagrams in Figure 3; all crystals plot firmly in the quadrilateral field of a Q–J diagram (Morimoto et al, 1988). In Figure 3A we follow the established convention of Morimoto et al (1988) in calculating the Fe component (ΣFe*) as the sum of Fe^{2+}, Fe^{3+} and Mn. However, Fe^{3+} is not incorporated into any of the quadrilateral end-member components (diopside, Di, $CaMgSi_2O_6$; hedenbergite, Hd, $CaFe^{2+}Si_2O_6$; enstatite, En, $MgSiO_3$ or ferrosilite, Fs, $Fe^{2+}SiO_3$); quadrilateral components only incorporate divalent cations on their M2 and M1 sites. In Figure 3B we therefore show pyroxene quadrilaterals plotted with a modified Fe component ($\Sigma Fe^{\dagger}$) calculated from the sum of Fe^{2+} and Mn (with Fe^{2+} determined following Droop (1987)). Clinopyroxene crystals from each of our OIB samples define distinct populations in both Figures 3A and 3B.

Clinopyroxene crystals in tholeiitic samples from Laki, Holuhraun and Skuggafjöll define an approximate crystal line of decent (Figure 3A), with those from Skuggafjöll being the most primitive (i.e., having the highest Di content), those from Holuhraun being slightly more evolved, and those from Laki being the most evolved (i.e., having the lowest Di content). Although Di and Hd dominate, all clinopyroxene crystals from tholeiitic basalts contain some En and Fs that increase in abundance with increasing degrees of evolution as Mg and Fe contents decrease and increase, respectively. Clinopyroxene crystals from Skuggafjöll show the greatest variability in DiHd (Di+Hd) and EnFs (En+Fs) contents, consistent with the presence of sector zoning described in greater detail below (Neave et al, 2019). Clinopyroxene crystals from Laki show the greatest overall spread in compositions, consistent with the protracted magmatic history recorded by these crystals (Neave et al, 2013). Removing Fe^{3+} from the calculation of quadrilateral components has no significant effect beyond moving all data slightly towards the Di vertex.

Despite erupting from two geographically distinct systems, clinopyroxene crystals in alkali samples from Pico and Eyjafjallajökull also define an approximate crystal line of descent (Figure 3A). Although the most primitive clinopyroxene crystals from

Eyjafjallajökull and Pico (and PI-011 in particular) lie close to some crystals from the tholeiitic Skuggafjöll eruption in quadrilateral space, evolved clinopyroxene crystals from Eyjafjallajökull and Pico (PI-041 in particular) lie much closer to the Di-Hd tie line than evolved clinopyroxene crystals from the tholeiitic Holuhraun and Laki eruptions. That is, clinopyroxene crystals from alkali samples seem to evolve towards higher DiHd, while those from tholeiitic samples evolve to lower DiHd. This effect is especially pronounced when Fe^{3+} is removed from the calculation of quadrilateral components and clinopyroxene compositions move towards the Di vertex (Fig 3B). Some clinopyroxene crystals from PI-041 fall above the Di-Hd tie line in this case, likely because of the greater contribution of Ca to non-quadrilateral components in clinopyroxene crystals from alkali samples with respect to those from tholeiitic samples (e.g., Robinson, 1980).

Clinopyroxene crystals from alkali samples contain higher Na_2O contents than those from tholeiitic samples (∼0.30–0.60 wt.% versus ∼0.15–0.30 wt.%; Figure 4A). Overall, there is a strong correlation between MgO and Na_2O, though clinopyroxene crystals from different eruptions fall on slightly offset arrays. Although significant (>1 wt.%) concentrations of Cr_2O_3 are only found in relatively primitive clinopyroxene crystals (Figure 4B), analyses from both alkali and tholeitiic samples define the same broad trend; evolved clinopyroxene crystals contain negligible Cr_2O_3. Clinopyroxene crystals from different eruptions are characterised by different Ti:Al values that are often remarkably constant within the products of any individual eruption. in general, clinopyroxene crystals from alkali samples have higher Ti:Al values than those from tholeiitic samples, with the exception of clinopyroxene crystals from the evolved and tholeiitic Laki eruption that overlap with clinopyroxene crystals in alkali ankaramite samples from Eyjafjallajökull.

Iron valence systematics

The concentration and valence systematics of Fe in clinopyroxene crystals from our OIB samples are summarised in Figure 5. Distinct crystal lines of descent identified on pyroxene quadrilaterals are reproduced on a plot of MgO versus total Fe expressed as FeO (FeO_T; Figure 5A). Clinopyroxene crystals in tholeiitic samples from Skuggafjöll, Holuhraun and Laki define a relatively steep trend in increasing FeO_T with decreasing MgO (with the highest FeO_T contents found in clinopyroxene rims from Laki), while clinopyroxene crystals in alkali samples from Pico define a shallower trend; crystals from Eyjafjallajökull fall between these two trends. However, relationships are weaker when MgO is plotted against FeO determined by stoichiometry following Droop (1987) (Figure 5B). For example, clinopyroxene crystals in samples from Skuggafjöll and Laki contain ∼1 and ∼2 wt.% less FeO than FeO_T, respectively, while FeO and FeO_T are broadly comparable in the sample from Holuhraun. Conversely, the enrichment in FeO with decreasing MgO is markedly less coherent than the enrichment in FeO_T.

Clinopyroxene Fe_2O_3 contents determined following Droop (1987) are summarised as a function of MgO in Figure 5C. Clinopyroxene Fe_2O_3 contents vary from within uncertainty of 0 wt.%, where 1σ uncertainties of ∼0.35 wt.% were obtained using a Monte Carlo approach described by Neave et al (2024), to ∼4.5 wt.%, highlighting that Fe_2O_3 is a significant constituent of many clinopyroxene crystals from OIBs. Alongside

Al, Fe^{3+} is therefore probably the most abundant cation in magmatic clinopyroxene crystals after those responsible for forming quadrilateral components (i.e., Si, Ca, Mg and Fe^{2+}). Overall, Fe_2O_3 contents are much lower in primitive clinopyroxene crystals with high MgO contents (∼1 wt.% at 17 wt.% MgO) than evolved clinopyroxene crystals with low MgO contents (∼4 wt.% at 13 wt.% MgO). To first order, clinopyroxene crystals from tholeiitic and alkali systems lie on the same MgO-Fe_2O_3 trend. In detail some finer structure arises. For example, clinopyroxene crystals in the Holuhraun sample contain the lowest Fe_2O_3 contents, which rarely exceed 1 wt.% and are often within uncertainty of 0 wt.%; clinopyroxene crystals from Skuggafjöll contain ∼1 wt.% more Fe_2O_3 than those from Holuhraun. Many clinopyroxene crystals in alkali samples are relatively evolved and contain high Fe_2O_3 contents that overlap with values from Skuggafjöll and Laki (1–2 wt.%) at their lower limits but extend to much higher values (∼4.5 wt%) at their upper limits. On average, clinopyroxene crystals in samples from Eyjafjallajökull reach any given Fe_2O_3 content at a higher MgO content than those from Pico. Rim and microcryst compositions from sample PI-041 extend from the main trend to low Fe_2O_3 (within uncertainty of 0 wt.%) at a constant MgO (∼13 wt.%).

Clinopyroxene $Fe^{3+}/\Sigma Fe$ contents estimated following the stoichiometric approach of Droop (1987) are summarised as a function of MgO in Figure 5D. These $Fe^{3+}/\Sigma Fe$ contents are typically subject to 1σ uncertainties of ∼0.03 according to a Monte Carlo approach described by Neave et al (2024). Clinopyroxene $Fe^{3+}/\Sigma Fe$ contents extend from ∼0.0–0.3 in primitive crystals in samples from Skuggafjöll and Holuhraun, with the latter having lower values mostly limited to 0.0–0.1, to ∼0.4 and ∼0.5 in evolved crystals in samples from Eyjafjallajökull and Pico, respectively. Importantly, these high values are consistent with high-precision analyses of clinopyroxene crystals in mafic alkali rocks from the Canary Islands by Mössbauer spectroscopy that yielded $Fe^{3+}/\Sigma Fe$ contents of 0.49–0.63 (Weis et al, 2015). Variations in $Fe^{3+}/\Sigma Fe$ are nonetheless considerable at any given MgO for any given eruption (≥0.3). However, in contrast with McGuire et al (1989) who ascribed similarly variable clinopyroxene $Fe^{3+}/\Sigma Fe$ contents to inadequacies in stoichiometric determinations of Fe^{3+}, we believe that much of this variability is geological in origin. Our reasons for this are threefold: firstly, the close correspondence between $Fe^{3+}/\Sigma Fe$ contents determined by Mössbauer and stoichiometry in endmember and single-crystal clinopyroxenes suggests that the latter can be reliable when EPMA performed with sufficient care (Neave et al, 2024); secondly, Monte Carlo-derived estimates of uncertainties in $Fe^{3+}/\Sigma Fe$ are smaller than the variability observed (1σ uncertainties of ∼0.03 are an order of magnitude smaller than natural variability of ≥0.3 at any given MgO); and finally, our knowledge of clinopyroxene chemistry has grown considerably in recent decades. In particular, we now have a much greater understanding of how kinetics and sector zone development generate compositional variability independently of magmatic evolution and magma storage conditions, especially when considering the abundance and systematics of trivalent Al that may also mediate the incorporation of similarly trivalent Fe^{3+} (Mollo et al, 2010, 2018; Neave et al, 2019; Ubide et al, 2019; Neave et al, 2024).

Compositional zoning in major elements and iron valence

Magmatic clinopyroxene crystals are often characterised by complex internal zoning (Dowty, 1976; Neave et al, 2019; Caricchi et al, 2020; Musu et al, 2023). Compositional variations associated with three distinct types of clinopyoxene zoning observed in our OIB samples are summarised in Figures 6–8. Hourglass sector zoning occurs in diverse magmatic clinopyroxene crystals, and is generally characterised by the differential partitioning of elements between $\{hk0\}$ prism sectors and $\{\bar{1}11\}$ hourglass sectors , though the nature and extent of this differential partitioning depends on bulk composition, cooling rate and the degree of undercooling (Leung, 1974; Kouchi et al, 1983; Neave et al, 2019). Although some recent studies have incorporated Fe^{3+} into their discussions of clinopyroxene zoning (Mollo et al, 2018; Ubide et al, 2019), the interplay between sector zoning and Fe valence systematics remains to be explored in detail.

Paired compositional profiles through low-BSE-intensity hourglass and high-BSE-intensity prism sectors in clinopyroxene crystals from our Skuggafjöll samples are shown in Figure 6; similar zoning is present in clinopyroxene crystals from the Holuhraun sample but is less intense. Low-BSE-intensity hourglass sectors are characterised by consistently lower Al_2O_3 and $Fe^{3+}/\Sigma Fe$ contents than high-BSE-intensity prism sectors, in line with published observations from geochemically similar samples from the Holuhraun eruption (Neave et al, 2019; Caricchi et al, 2020) and considerably more alkaline samples from Mt Etna, Italy (Ubide et al, 2019; Musu et al, 2023).

Compositional profiles through clinopyroxene crystals with concentric (i.e., core-to-rim) zoning in sample PI-041 from Pico are shown in Figure 7. Crystal interiors only show modest variability in Mg# (where Mg# = molar $Mg/(Mg+Fe^{2+})$) or $Fe^{3+}/\Sigma Fe$ contents that largely reflects propagated analytical uncertainties. Core-to-rim zoning in these crystals is most clearly reflected in changes in TiO_2 contents; changes in Mg# and Al_2O_3 are more subtle. Moreover, there are no coherent changes in $Fe^{3+}/\Sigma Fe$ contents across core-rim boundaries, suggesting that $Fe^{3+}/\Sigma Fe$ zoning can be decoupled from zoning in other components.

Coarse compositional profiles through large clinopyroxene crystals with patchy sector zoning in sample PI-011 from Pico are shown in Figure 8. Mg#, TiO_2 and Al_2O_3 show coupled variability beyond analytical uncertainty. Variability in $Fe^{3+}/\Sigma Fe$ also exceeds analytical uncertainty though there is no clear relationship between Al_2O_3 and $Fe^{3+}/\Sigma Fe$ like there is in the crystals with hourglass sector zoning described above and shown in Figure 6. Nonetheless, correlated variability in TiO_2 and Al_2O_3 suggests that the patchy sector zoning in these crystals may result from the same crystallographic controls as hourglass sector zoning (Leung, 1974; Ubide et al, 2019), even if the extent to which this variability is coupled to $Fe^{3+}/\Sigma Fe$ differs between samples.

Discussion

Clinopyroxene chemical systematics

Clinopyroxene components calculated following the scheme described by Neave et al (2024) are plotted as functions of clinopyroxene Mg# in Figure 9 (a summary of the

scheme is provided in the appendix). There is considerable variability within and between clinopyroxene crystals from different OIB samples. Clinopyroxene crystals from tholeiitic samples contain similar amounts of Jd, while the Jd content in crystals from alkali samples is larger and more variable (Figure 9A). Although it is unsurprising that clinopyroxene crystals from alkali-rich systems contain more Na-bearing Jd than those from tholeiitic systems, differences in Jd contents also reflect differences in magma storage pressures. Both Jd-based clinopyroxene-liquid barometry and clinopyroxene-independent volatile saturation barometry indicate that the tholeiitic magmas erupted at Skuggafjöll, Holuhraun and Laki were stored at lower pressures prior to eruption (∼200 MPa; Neave and Putirka, 2017; Bali et al, 2018) than the alkali magmas erupted from Pico (200–600 MPa; Zanon et al, 2020; van Gerve et al, 2024). The broadly intermediate Jd content of clinopyroxene crystals from Eyjafjallajökull reflects their intermediate storage depths (∼300 MPa; Nikkola et al, 2019). As anticipated, relatively few clinopyroxene crystals contain much Ae (Figure 9B), with any Ae present restricted to ^{VI}Al-poor analyses from Na-rich or low-Mg# crystals. Otherwise, there are no clear systematics in the Ae content of clinopyroxene crystals in our OIB samples. In contrast with the inferences of Lindsley (1983), Fe^{3+} does not appear to be hosted by Ae in most magmatic clinopyroxene crystals, aegirine and aegirine-augite crystals from evolved alkali systems notwithstanding (cf., Larsen, 1976; White et al, 2005).

In line with their high Fe^{3+} but low Ae contents, we infer that Es is a major constituent of clinopyroxene crystals in our OIB samples (Figure 9C). With the exception of some very Fe^{3+}-poor analyses in our Holuhraun sample ($X_{Es} \sim 0$) that are mainly found within $\{\bar{1}11\}$ hourglass sectors (Figure 6), the Es content of clinopyroxene crystals from tholeiitic and alkali samples largely overlap, with the latter extending to slightly higher values (∼0.07 versus ∼0.10). Indeed, much of the spread in clinopyroxene Es contents at any given Mg# likely reflects the differential partitioning of Es between sectors as well as propagated uncertainties in clinopyroxene Fe^{3+} contents (Figure 6; Ubide et al, 2019). The tempering of high Es contents in the highest-Fe^{3+} clinopyroxene crystals from alkali samples reflects the formation of minor Ae in some cases (Figure 9B). Overall, it is likely that Es is the most abundant non-quadrilateral component in most clinopyroxene crystals from our OIB samples. Although the Es content of clinopyroxene crystals does not correlate straightforwardly with clinopyroxene Mg# (Figure 9C), Fe_2O_3 correlates negatively with MgO (Figure 5C) on a sample-by-sample basis. While relationships between MgO and Fe_2O_3 are complicated by the details of partitioning behaviour (see below), we note that a broad increase in clinopyroxene Fe_2O_3 with increasing differentiation may partly reflect the progressive enrichment of magmas in Fe_2O_3 following the crystallisation of Fe^{3+}-poor phases. Indeed, such so-called auto-oxidation has been described in experiments on calc-alkaline magmas (Ulmer et al, 2018), and has been invoked to explain the apparent oxidation of evolving MORBs (O'Neill et al, 2018).

The abundance of calcium Tschermak's component (CaTs, $CaAlAlSiO_6$) varies considerably between clinopyroxene crystals in different samples (Figure 9D). Clinopyroxene crystals in our samples from Skuggafjöll and alkali systems have large ranges in CaTs contents (0.00–0.05), which reflects the prevalence of sector zoning, hourglass

and patchy, in these samples (Figures 6 and 8). Such zoning is largely defined by the partitioning of quadrilateral and non-quadrilateral components between different sectors (Neave et al, 2019; Ubide et al, 2019). Crystals from our Laki sample are poor in CaTs, likely because of their relatively high Fe_2O_3 contents such that ^{IV}Al is balanced by Fe^{3+} rather than ^{IV}Al, consistent with the high FeO_T content of the Laki lava as a whole (Passmore et al, 2012). In contrast, crystals from our Holuhraun sample are relatively rich in CaTs, consistent with their low Fe_2O_3 contents. Although high CaTs contents can reflect disequilibrium crystallisation in some clinopyroxenes, this does not appear to be the case in crystals from Holuhraun (Neave et al, 2019).

The abundance of titanium pyroxene component (CaTi, $CaTiAl_2O_6$) varies significantly between samples (Figure 9E). Clinopyroxene crystals in tholeiitic samples define an approximate differentiation trend at relatively low CaTi for any given Mg# (evolving from ∼0.01 at Mg# = 0.90 to ∼0.04 at Mg# = 0.75), while clinopyroxene crystals in alkali samples from Pico evolve towards much higher CaTi (from ∼0.02 at Mg# = 0.90 to ∼0.08 at Mg# = 0.75). Clinopyroxene crystals in samples from Eyjafjalljökull define a somewhat intermediate trend that partly overlaps with the trend defined by crystals in samples from Pico. These trends not only reflect the way in which clinopyroxene Ti contents track magmatic evolution, but also the close association between Ti and Al in clinopyroxene crystals from alkali magmas that is generally conserved across sector zones (Leung, 1974; Downes, 1974; Ubide et al, 2019). The incorporation of Ti alongside $2^{IV}Al$ is consistent with the Ti:Al ratios in excess of 1:2 that are observed in all samples (Figure 4C), where excess Al remaining after CaTi formation can form other components including Jd, Es and CaTs. We also note that calculating CaTi from Ti rather than residual ^{IV}Al as suggested by Putirka et al (1996) is essential for recovering clinopyroxene Ti systematics accurately; calculating from ^{IV}Al could overestimate apparent CaTi contents. Although there is no need to form other Ti-bearing components such as Ti-diopside ($CaMgTi_2O_6$), neptunite ($NaFe^{2+}_{0.5}Ti_{0.5}Si_2O_6$), its Mg-bearing equivalent ($NaMg_{0.5}Ti_{0.5}Si_2O_6$) or the fictive alumino-buffonite ($CaMg_{0.5}Ti_{0.5}AlSiO_6$) of Sack and Ghiorso (1994) to account for the compositions of our clinopyroxene crystals, there is ample scope for further substitutions that are not captured by the componentry scheme of Neave et al (2024). Addressing this complexity would however require a thermodynamic approach that is beyond the scope of this manuscript.

Significant amounts of chromian calcium-Tschermak's component (CrAlTs, $CaCrAlSiO_6$) only occur in high-Mg# clinopyroxene crystals (Figure 9F). This is consistent with the relative compatibility of Cr in clinopyroxene and its relatively low abundance in OIB magmas. Thus, CrAlTs contents rapidly decrease from ∼0.030 to <0.005 over a Mg# window of ∼0.90 to 0.75 in clinopyroxene crystals from both tholeiitic and alkali samples. High CrAlTs contents are offset to higher Mg# in clinopyroxene crystals from Pico and Eyjafjallajökull then their tholeiitic equivalents because the higher Fe^{3+} content of these crystals leads to higher Mg# values at any given Mg content.

As anticipated, all clinopyroxene crystals in our OIB samples are dominated by DiHd (Figure 9G). It is notable that the DiHd contents of clinopyroxene crystals from

tholeiitic samples are generally lower than those from our alkali samples (0.64–0.76 versus 0.70–0.80, respectively). The DiHd content of clinopyroxene crystals from tholeiitic samples also decreases with decreasing Mg# in a manner consistent with the pyroxene solvus between DiHd and EnFs narrowing with decreasing temperature (Lindsley and Andersen, 1983). In contrast, the DiHd content of clinopyroxene crystals from alkali samples remains broadly constant with decreasing Mg#. Importantly, calculating DiHd in this manner accounts for the incorporation of Ca into non-quadrilateral components, meaning we do not observe the excess DiHd implied from pyroxene quadrilaterals shown in Figure 3B that account for Fe^{3+} but not non-quadrilateral Ca; the high and steady DiHd content with decreasing Mg# in clinopyroxene crystals from alkali samples appears to be real. Unsurprisingly, EnFs contents of our clinopyroxene crystals are almost perfectly antithetical to their DiHd contents, with the striking observation that X_{EnFs} does not increase with decreasing Mg# in clinopyroxene crystals from alkali samples.

Ferric iron partitioning

The presence of significant Fe^{3+} in clinopyroxene crystals from diverse OIB samples demonstrates that the valence state of Fe can no longer be ignored in robust descriptions of magmatic evolution that draw on clinopyroxene chemistry. It also implies that clinopyroxene crystals may record widespread but currently under-exploited archives of magmatic $f_{\mathrm{O_2}}$. Indeed, the potential for clinopyroxene oxybarometry has been demonstrated for mantle samples investigated by Mössbauer spectroscopy (Luth and Canil, 1993). However, poorly defined steric constraints on Fe^{3+} incorporation into clinopyroxene mean that it is currently impossible to extend oxybarometric approaches based on olivine-liquid Fe^{2+}–Mg exchange equilibria described by $K^{\mathrm{ol-liq}}_{\mathrm{D,Fe^{2+}-Mg}}$ values to clinopyroxene-liquid Fe^{2+}–Mg exchange equilibria (Blundy et al, 2020; Davis and Cottrell, 2021; Saper et al, 2022). Thus, a vital step towards understanding the effects of magmatic $f_{\mathrm{O_2}}$ on clinopyroxene compositions involves exploring the systematics of Fe^{3+} partitioning between clinopyroxene crystals and magmatic liquids.

Samples from Holuhraun, Skuggafjöll and Pico (PI-041) contain clinopyroxene crystals in textural equilibrium with their host glasses and are thus suitable for investigating Fe^{3+} partitioning. Clinopyroxene analyses from Skuggafjöll and Holuhraun were filtered to only include high-Al_2O_3 analyses from $\{hk0\}$ sectors that grew under near-equilibrium conditions (Halldórsson et al, 2018; Neave et al, 2019); $\{\bar{1}11\}$ sectors did not form under equilibrium conditions and were thus considered unsuitable for investigating Fe^{3+} partitioning. Rim and microcryst analyses feasibly in equilibrium with the matrix glass of PI-041 were identified texturally; compositionally distinct rims in contact with glasses are clear in clinopyroxene crystals from PI-041 (Figures 2F and 7) and appear unaffected by sector zoning.

The Al_2O_3 and Fe_2O_3 contents of clinopyroxene analyses in textural equilibrium with their host glasses are shown in Figure 10; analyses with $Fe_2O_3 < 0.35$ have been removed as they lie below the effective detection limit of stoichiometric determinations. Analyses from our Holuhraun sample show minimal variability, while those from both PI-041 and our Skuggafjöll samples are much more variable. Having eliminated effects from sector zoning, elevated and somewhat correlated Fe_2O_3 and Al_2O_3 contents likely

reflect the enhanced incorporation of trivalent cations via Tschermak-type substitutions during disequilibrium crystallisation (Mollo et al, 2010; Ubide et al, 2019). That is, while the clinopyroxene analyses we selected appear to be in textural equilibrium with their host glasses, only some of them are in chemical equilibrium.

In order to convert our observed clinopyroxene Fe_2O_3 contents into Fe^{3+} partition coefficients (i.e., $D^{cpx-liq}_{Fe_2O_3}$ values) we estimated the $Fe^{3+}/\Sigma Fe$ content of glasses in our Skuggaföll, Holuhraun and Pico (PI-041) samples from olivine-liquid equilibria (Figure 11). Specifically, we determined glass $Fe^{3+}/\Sigma Fe$ contents from olivine rims and microcrysts by using Equation 10 of Saper et al (2022) to calculate appropriate values of $K^{ol-liq}_{D,Fe^{2+}-Mg}$ from which glass Fe^{2+} contents and Mg# values could be estimated (Figure 11A). Glass $Fe^{3+}/\Sigma Fe$ contents were then converted into f_{O_2} conditions using the model of Borisov et al (2018), and are reported as log-unit deviations from FMQ in Figure 11B. Best estimates of glass $Fe^{3+}/\Sigma Fe$ in our Skuggafjöll and Holuhraun samples of ∼0.19 are similar to values reported from other Icelandic tholeiites from Fe-XANES spectroscopy (up to 0.20 for Laki; Hartley et al, 2017). A glass $Fe^{3+}/\Sigma Fe$ content of ∼0.19 corresponds to an f_{O_2} of FMQ+1, which is broadly consistent with S systematics in the products of the Holuhraun eruption that indicate an f_{O_2} of ∼FMQ+0.5 (Bali et al, 2018). Olivine crystals from PI-041 return higher glass $Fe^{3+}/\Sigma Fe$ contents of ∼0.33 that correspond to an f_{O_2} of ∼FMQ+2.5, in line with glass $Fe^{3+}/\Sigma Fe$ maxima observed in OIB samples erupted elsewhere (Brounce et al, 2017; Moussallam et al, 2019). These values are also comparable to the results of V-in-olivine oxybarometry performed on petrologically similar samples from El Hierro in the Canary Islands (Taracsak et al, 2022). While subject to analytical uncertainties, our olivine-based approach nonetheless provides plausible and internally consistent estimates of glass $Fe^{3+}/\Sigma Fe$ that enable deeper investigations of clinopyroxene-liquid Fe^{3+} partitioning.

Estimated $D^{cpx-liq}_{Fe_2O_3}$ values are summarised as a function of clinopyroxene Al_2O_3 in Figure 12A. While each of the clinopyroxene populations considered form a distinct cluster on Figure 12A, little overall structure is apparent. Analyses from our Holuhraun sample lie to low Al_2O_3 and low $D^{cpx-liq}_{Fe_2O_3}$, while those from our Skuggafjöll samples lie to low Al_2O_3 but with a large range in $D^{cpx-liq}_{Fe_2O_3}$ and those from Pico span wide ranges in Al_2O_3 and $D^{cpx-liq}_{Fe_2O_3}$. However, when $D^{cpx-liq}_{Fe_2O_3}$ values are instead summarised as a function of ^{IV}Al, which forms Es alongside Fe^{3+} via the coupled substitution $(Mg,Fe^{2+}) + Si = Fe^{3+} + {}^{IV}Al$, some structure can be resolved. Correlated variations in $D^{cpx-liq}_{Fe_2O_3}$ and ^{IV}Al in our tholeiitic and alkali samples can be fitted with separate linear models of modest quality ($r^2 = 0.35$ and 0.32, respectively). Nonetheless, our observations suggest that ^{IV}Al plays a key role in mediating Fe^{3+} incorporation into magmatic clinopyroxene crystals, and that the nature of this effect depends on clinopyroxene composition. The shallower slope of the regression through crystals from alkali samples with respect to that through crystals from tholeiitic samples likely reflects the incorporation of greater amounts of Ti as CaTi (i.e., $CaTiAl_2O_6$) in the former.

Published estimates of $D^{cpx-liq}_{Fe_2O_3}$ are shown in Figure 12. Mallmann and O'Neill (2009) and Davis and Cottrell (2021) report constant values of 0.453±0.158 and

0.78±0.30, respectively, while McCanta et al (2004) report values in the range 0.00–0.77. Iron was only present at trace levels in the (near-)CMAS experiments of Mallmann and O'Neill (2009), casting doubt on the suitability of using their estimated $D^{cpx-liq}_{Fe_2O_3}$ value to describe Fe^{3+} partitioning in OIB samples where Fe_2O_3 is a major constituent (>1 wt.%), despite overlapping with our observations from natural samples. Davis and Cottrell (2021) investigated Fe^{3+} partitioning in ultramafic but nevertheless Fe-poor systems, deriving $D^{cpx-liq}_{Fe_2O_3}$ indirectly through Fe^{2+}–Mg exchange between olivine and clinopyroxene. While Davis and Cottrell (2021) inferred that $D^{cpx-liq}_{Fe_2O_3}$ was not affected by f_{O_2} in their variable f_{O_2} experiments, there is insufficient chemical variability in their experimental clinopyroxene crystals to identify potential chemical controls over Fe^{3+} partitioning. That is, the clinopyroxene crystals they used to estimate $D^{cpx-liq}_{Fe_2O_3}$ have very similar Al_2O_3 and ^{IV}Al contents, so any potential mediation of Fe^{3+} incorporation by Al_2O_3 or ^{IV}Al cannot be evaluated. The $D^{cpx-liq}_{Fe_2O_3}$ values reported by Davis and Cottrell (2021) are nonetheless consistent with our linear model through clinopyroxene analyses from tholeiitic samples (Figure 12B).

McCanta et al (2004) report values of 0.00–0.77 from their experiments on a SNC meteorite composition, with values of 0.00–0.09 being obtained under reducing conditions when Fe^{3+} will be essentially absent (∼FMQ−4.7 to FMQ−2.7) and elevated values of 0.48–0.77 being obtained under conditions approaching those relevant for terrestrial magmatism (∼FMQ−0.7 to ∼FMQ+0.3). Unfortunately McCanta et al (2004) do not provide the compositional information required to assess whether their reported variations in $D^{cpx-liq}_{Fe_2O_3}$ reflect changes in f_{O_2} alone, or whether clinopyroxene compositions also play a role. Moreover, the Fe^{3+} contents of augite crystals measured by McCanta et al (2004) were subject to 1σ uncertainties similar in magnitude to the Fe^{3+} contents themselves, and as such their reported $D^{cpx-liq}_{Fe_2O_3}$ values should be considered similarly uncertain.

Overall, our observations indicate that $D^{cpx-liq}_{Fe_2O_3}$ values in OIB systems likely range between 0.2 and 1.0 depending on the composition of the clinopyroxene and liquid in question. Clinopyroxene ^{IV}Al contents appear to play a central role in meditating their Fe^{3+} contents, but the strength of this effect depends on system alkalinity, with clinopyroxene crystals in alkali systems incorporating less Fe^{3+} for any given increase in ^{IV}Al than those from tholeiitic systems, likely because of the coupled incorporation of Ti. Importantly, if the partitioning of Fe^{3+} is linked to the incorporation of ^{IV}Al, then clinopyroxene Fe_2O_3 contents will be similarly sensitive to disequilibrium crystallisation as their Al_2O_3 and TiO_2 contents (Mollo et al, 2010, 2013; Ubide et al, 2019). That is, coupled increases in clinopyroxene Fe_2O_3, Al_2O_3 and TiO_2 contents likely result from disequilibrium processes such that apparent $D^{cpx-liq}_{Fe_2O_3}$ values may not always truly reflect equilibrium Fe^{3+} partitioning, even when considering compositions from $\{hk0\}$ prism sectors most likely to record equilibrium conditions. A key implication of this is that the lower end of our estimated $D^{cpx-liq}_{Fe_2O_3}$ ranges probably represent our best estimates of equilibrium partitioning (i.e., ∼0.2 for the tholeiitic samples and ∼0.4 for the alkali sample). Nonetheless, our estimated $D^{cpx-liq}_{Fe_2O_3}$ values

are broadly in line with the sparse experimental observations available, though additional experimental work is still required to develop robust and predictive descriptions of Fe^{3+} partitioning between clinopyroxene and liquid.

Iron-magnesium exchange equilibria

Clinopyroxene crystals primarily record magmatic evolution in a transition from high-Mg# compositions dominated by Di to low-Mg# compositions that are relatively enriched in Hd. As such, clinopyroxene-liquid equilibria are often summarised in terms of Fe^{2+}–Mg exchange (Wood and Blundy, 1997; Putirka, 2008). This convention at least partly reflects similarities between clinopyroxene-liquid equilibria described using $K^{cpx-liq}_{D,Fe^{2+}-Mg}$ values and olivine-liquid equilibria described using $K^{ol-liq}_{D,Fe^{2+}-Mg}$ values (Roeder and Emslie, 1970; Blundy et al, 2020; Saper et al, 2022). Equation 35 of Putirka (2008) provides the most recent model capable of predicting $K^{cpx-liq}_{D,Fe-Mg}$ values that is feasibly applicable to OIB samples. Although this model incorporates the effect of temperature on $K^{cpx-liq}_{D,Fe-Mg}$, and returns a value of ∼0.28 at temperatures relevant to OIB evolution (∼1200 °C) that is close to values from experiments on mafic compositions (0.25–0.26; Sisson and Grove, 1993; Salazar-Naranjo and Vlach, 2023), it assumes that all Fe occurs as Fe^{2+} in both clinopyroxene crystals and their host glasses and thus strictly describes Fe–Mg exchange rather than $Fe^{2+} - -Mg$ exchange specifically. This assumption is clearly incorrect for basaltic liquids characterised by $Fe^{3+}/\Sigma Fe$ contents that range from ∼0.1 to ∼0.3 across a naturally relevant range of f_{O_2} conditions (FMQ−1 to FMQ+2; Kress and Carmichael, 1991; Borisov et al, 2018; Cottrell et al, 2022). Our findings also demonstrate that this assumption is incorrect from the crystal perspective, with clinopyroxene crystals in diverse OIB samples exhibiting $Fe^{3+}/\Sigma Fe$ contents ranging from ∼0.0 to ∼0.5 (Figure 5D). Given that Fe^{2+} and Fe^{3+} are incorporated into clinopyroxene within quadrilateral and non-quadrilateral components, respectively, Fe^{3+} is unlikely to substitute directly with Mg or Fe^{2+} (e.g., Ubide et al, 2019; Neave et al, 2024), meaning that Fe^{2+}–Mg exchange may be only indirectly affected by Fe^{3+}. Improving our ability to interpret observations from clinopyroxene crystals in natural and experimental systems thus requires clinopyroxene-liquid Fe^{2+}–Mg exchange equilibria and $K^{cpx-liq}_{D,Fe^{2+}-Mg}$ systematics *sensu stricto* to be investigated in greater depth.

Samples from Skuggafjöll, Holuhraun and Pico (PI-041) contain clinopyroxene crystals in textural equilibrium with their host glasses and are suitable for investigating Fe^{2+}–Mg exchange in detail. Combined glass and clinopyroxene Mg# systematics are summarised in Figure 13. Clinopyroxene-liquid Fe–Mg exchange equilibria were first calculated following current recommendations that all Fe should be taken as Fe^{2+} in both clinopyroxene and liquid (Wieser et al, 2023a,b). These calculations return $K^{cpx-liq}_{D,Fe-Mg}$ values within uncertainty (±0.08 1σ) of, but also consistently lower than, the 0.28 value calculated with Equation 35 of Putirka (2008). This suggests either that our clinopyroxene crystals do not record equilibrium or that ignoring Fe^{3+} creates a systematic bias between $K^{cpx-liq}_{D,Fe-Mg}$ and $K^{cpx-liq}_{D,Fe^{2+}-Mg}$ values, assuming that equilibrium values of $K^{cpx-liq}_{D,Fe^{2+}-Mg}$ are indeed close to 0.28.

Clinopyroxene-liquid Fe^{2+}–Mg exchange equilibria were subsequently calculated with clinopyroxene Fe^{2+} contents determined by stoichiometry following Droop (1987) and liquid (i.e., glass) Fe^{2+} contents fixed at a range of relevant f_{O_2} conditions (FMQ to FMQ+3) according to the model of Borisov et al (2018). Accounting for the presence of Fe^{3+} increases both glass and clinopyroxene Mg# values. However, the magnitudes of Mg# increases vary within and between samples because clinopyroxene Fe_2O_3 contents also vary (Figure 5C). Best estimates of clinopyroxene-liquid Fe^{2+}–Mg exchange equilibria in our samples were then evaluated using two approaches. In the first approach, mean clinopyroxene compositions were assumed to be in equilibrium with glass $Fe^{3+}/\Sigma Fe$ contents estimated from olivine-liquid equilibria (Figure 11), ∼0.19 for samples from Skuggafjöll and Holuhraun and ∼0.33 for sample PI-041 from Pico. In the second approach, applied to samples from Skuggafjöll and Pico (PI-041), the same glass compositions were assumed to be in equilibrium with the lowest-Mg# clinopyroxene compositions in each population because they are least likely to be the products of disequilibrium crystallisation.

The best estimate of clinopyroxene-liquid Fe^{2+}–Mg equilibrium calculated from the mean clinopyroxene composition in our Holuhraun sample is consistent with a $K^{cpx-liq}_{D,Fe^{2+}-Mg}$ value of ∼0.28 (Figure 13B). The relative homogeneity of $\{hk0\}$ sectors in clinopyroxene crystals from the Holuhraun sample suggests that they formed under near-equilibrium conditions, sector zoning notwitstanding (Neave et al, 2019; Caricchi et al, 2020), and that $K^{cpx-liq}_{D,Fe^{2+}-Mg}$ was indeed close to 0.28, broadly consistent with experimental observations on chemically similar systems (∼0.26; Sisson and Grove, 1993). Moreover, coherence between olivine-liquid and clinopyroxene-liquid equilibria suggest that the Holuhraun magma evolved under f_{O_2} conditions close to FMQ+1, in general agreement with estimates from independent methods (∼FMQ+0.5; Bali et al, 2018).

The best estimate of clinopyroxene-liquid Fe^{2+}–Mg equilibrium calculated from the mean clinopyroxene composition in our Skuggafjöll samples is consistent with a much lower $K^{cpx-liq}_{D,Fe^{2+}-Mg}$ value of ∼0.23 (Figure 13A), within model uncertainty of ∼0.28, but lower than experimentally observed values of ∼0.26 (Sisson and Grove, 1993). If taken at face value, the mean clinopyroxene composition is thus consistent with a $K^{cpx-liq}_{D,Fe^{2+}-Mg}$ value of ∼0.28 at oxidising conditions of ∼FMQ+2.5. However, observations from elsewhere in Iceland and the Reykjanes Ridge suggest that such oxidising conditions are unrealistic for Icelandic tholeiites (Shorttle, 2015; Hartley et al, 2017; Bali et al, 2018; **?**). While the absence of distinct rim zones indicates that the clinopyroxene compositions considered here did indeed grow from their host glasses (Figure 2A), it is likely that some portions of $\{hk0\}$ prism sectors from the Skuggafjöll eruption grew under disequilibrium conditions during crystallisation at high degrees of undercooling (e.g., Mollo et al, 2010, 2013). The lowest-Mg# (i.e., lowest Fe^{3+}) clinopyroxene compositions least affected by disequilibrium crystallisation therefore provide the best estimate of clinopyroxene-liquid Fe^{2+}–Mg equilibrium in our Skuggafjöll samples: the lowest-Mg# clinopyroxene composition is broadly consistent with a $K^{cpx-liq}_{D,Fe^{2+}-Mg}$ value of ∼0.28 at an f_{O_2} of ∼FMQ+1. This value is in line with observations from our Holuhraun sample that was less impacted by disequilibrium crystallisation – mean- and lowest-Mg# clinopyroxene compositions from our

Holuhraun sample both return $K_{D,Fe^{2+}-Mg}^{cpx-liq}$ and f_{O_2} values close to 0.28 and FMQ+1, respectively.

Interpreting clinopyroxene-liquid Fe^{2+}–Mg equilibria in sample PI-041 from Pico is complex as different crystal populations appear to record growth under different conditions (Figure 13C). If we initially assume that mean clinopyroxene compositions recorded clinopyroxene-liquid equilibrium best, microcrysts record a $K_{D,Fe^{2+}-Mg}^{cpx-liq}$ value of ∼0.28 at a plausible f_{O_2} of ∼FMQ+2.5 (Figure 11), while rims record a seemingly disequilibrium $K_{D,Fe^{2+}-Mg}^{cpx-liq}$ value of ∼0.20. A $K_{D,Fe^{2+}-Mg}^{cpx-liq}$ value of ∼0.20 is not only at the limit of uncertainty in Equation 35 of Putirka (2008) but, more importantly, is also inconsistent with the value from microcrysts in the same sample. There are no textural indications why either rims or microcrysts should be discounted as potential archives of clinopyroxene-liquid equilibrium. However, their elevated and variable Fe_2O_3 and Al_2O_3 contents suggest that both rims and microcrysts grew under varying degrees of disequilibrium. As such, the lowest-Mg# clinopyroxene compositions in each population are likely to provide the best records of clinopyroxene-liquid Fe^{2+}–Mg equilibrium. In this case, clinopyroxene rims record a $K_{D,Fe^{2+}-Mg}^{cpx-liq}$ value of ∼0.25 at an f_{O_2} of ∼FMQ+2.5 inferred from olivine-liquid equilibria, which is much closer to ∼0.28 than the ∼0.20 value recorded by the mean rim composition. If f_{O_2} were closer to FMQ+3, then the $K_{D,Fe^{2+}-Mg}^{cpx-liq}$ value would be closer to a nominal value of ∼0.28. Recent experiments reported by Salazar-Naranjo and Vlach (2023) suggest that equilibrium $K_{D,Fe^{2+}-Mg}^{cpx-liq}$ values for alkali systems may actually lie closer to ∼0.25 than to the ∼0.28 value calculated from Equation 35 of Putirka (2008). Discordance between rims and microcrysts nonetheless remains, with the lowest-Mg# microcrysts implying a disequilibrium $K_{D,Fe^{2+}-Mg}^{cpx-liq}$ value greater than 0.36 at ∼FMQ+2.5. However, if rims and microcrysts formed at different times and under different f_{O_2} conditions they can be reconciled. It is well documented that SO_2 degassing during magma ascent leads to the reduction of magmatic liquids (Moussallam et al, 2016; Helz et al, 2017), with initially high-f_{O_2} alkali basalts (∼FMQ+3) recording f_{O_2} conditions at or below FMQ by eruption (Taracsak et al, 2022). We therefore speculate that the rims of clinopyroxene (and olivine) crystals in sample PI-041 from Pico formed under relatively high f_{O_2} conditions close to ∼FMQ+2.5 at depth prior to any significant SO_2 degassing. We suggest that clinopyroxene microcrysts then formed after significant SO_2 degassing occurred during ascent such that the lowest-Mg# microcrysts record a $K_{D,Fe^{2+}-Mg}^{cpx-liq}$ value of ∼0.28 under f_{O_2} conditions close to ∼FMQ.

Overall, our results illustrate that accounting for the presence of Fe^{3+} significantly impacts how clinopyroxene-liquid Fe^{2+}–Mg exchange equilibria in OIB samples are evaluated. Nonetheless, $K_{D,Fe-Mg}^{cpx-liq}$ values calculated assuming that all Fe is present as Fe^{2+} are generally within the (large) ±0.08 uncertainty of the general predictive model provided by Equation 35 of Putirka (2008). Once the effects of disequilibrium crystallisation are accounted for, our observations from natural OIB samples suggest that $K_{D,Fe^{2+}-Mg}^{cpx-liq}$ values lie close to 0.28 and are broadly consistent with experimentally derived $K_{D,Fe^{2+}-Mg}^{cpx-liq}$ values of 0.25–0.26 (Sisson and Grove, 1993; Salazar-Naranjo and Vlach, 2023). Moreover, different clinopyroxene populations within a single sample

(PI-041 from Pico) record different clinopyroxene-liquid Fe^{2+}–Mg systematics, potentially mirroring variations in f_{O_2} conditions reported from other OIB system that are thought to result from SO_2 degassing during ascent (Moussallam et al, 2016; Helz et al, 2017; Taracsak et al, 2022). Considerable uncertainties nevertheless remain in our interpretations. Targeted experiments are thus required to identify and disentangle the effects of composition, disequilibrium and f_{O_2} conditions on clinopyroxene-liquid Fe^{2+}–Mg exchange before we can calibrate a robust predictive model of $K_{D,Fe^{2+}-Mg}^{cpx-liq}$ for modelling and interpreting and OIB samples.

Conclusions

By applying the stoichiometric approach for determining clinopyroxene $Fe^{3+}/\Sigma Fe$ contents described by Droop (1987) to compositionally diverse OIB samples from Iceland and the Azores, we demonstrate that Fe^{3+} is one of the most abundant if underappreciated cations in magmatic clinopyroxene crystals from ocean island volcanoes. On average, clinopyroxene crystals from alkali systems have higher $Fe^{3+}/\Sigma Fe$ contents than those from tholeiitic systems, which translate into higher Es contents and, in some cases, non-negligible Ae contents. The incorporation of Ca and ^{IV}Al in clinopyroxene crystals alongside Fe^{3+} has important consequences for the relative proportions of other clinopyroxene components such as DiHd and EnFs. Trends in clinopyroxene Jd, CaTi and CrAlTs contents can be variably linked to magma composition (i.e., alkalinity), storage pressure and the degree of magmatic evolution. Clinopyroxene Es contents are somewhat related to the f_{O_2} conditions under which their carrier liquids evolved, with crystals from alkali systems that typically evolve under relatively oxidising conditions generally containing more Es than those from tholeiitic systems. However, clinopyroxene Es, CaTs and CaTi contents also reflect disequilibrium crystallisation during crystal growth in some samples. Sector zone development at modest degrees of undercooling leads to the crystallisation of disequilibrium compositions depleted in Es, CaTs and CaTi that are mainly associated with $\{\bar{1}11\}$ hourglass sectors; $\{hk0\}$ prism sectors are most likely to record equilibrium crystallisation conditions. Nevertheless, even the compositions of $\{hk0\}$ prism sectors may record disequilibrium compositions enriched in Es, CaTs and CaTi when crystallisation occurs under high degrees of undercooling. Overall, Fe^{3+} shows similar behaviour to Al and Ti during clinopyroxene crystallisation and its behaviour may thus be interpreted within a growing corpus of knowledge about the textural and chemical evolution of clinopyroxene crystals (Ubide et al, 2019; Neave et al, 2019).

By exploiting the ability to estimate glass $Fe^{3+}/\Sigma Fe$ contents from olivine-liquid equilibria, we investigated Fe^{3+} partitioning in a subset of our OIB samples with quenched matrix glasses. Olivine-liquid equilibria in tholeiitic samples from Skuggafjöll and Holuhraun record glass compositions consistent with f_{O_2} conditions of ∼FMQ+1, while those in the alkali sample PI-041 from Pico record compositions consistent with relatively oxidising f_{O_2} conditions of ∼FMQ+2.5. These values are consistent with observations from a range of ocean island settings, and potentially reinforce suggestions that OIBs with EMII affinities, like those from the Azores, evolve under more oxidising conditions than those with C/FOZO/PREMA affinities, like

those from Iceland (Brounce et al, 2022; Weis et al, 2023). Estimated $D^{cpx-liq}_{Fe_2O_3}$ values from clinopyroxene analyses in textural equilibrium with their host glasses fall in the range 0.2–1.0, and appear to be mediated by the abundance of ^{IV}Al. This implies that there are strong steric controls over the incoporation of Fe^{3+} into clinopyroxene, though the exact nature of ^{IV}Al-$D^{cpx-liq}_{Fe_2O_3}$ relationships differs between tholeiitic and alkali compositions. Much of the variability in apparent $D^{cpx-liq}_{Fe_2O_3}$ values in samples from Skuggafjöll and Pico may however record disequilibrium, with ^{IV}Al- and Fe^{3+}-rich analyses reflecting the enhanced incorporation of non-quadrilateral components during crystallisation at high degrees of undercooling; equilibrium $D^{cpx-liq}_{Fe_2O_3}$ values during magmatic evolution may thus lie towards the lower end of the 0.2–1.0 range (i.e., 0.2–0.4). While our findings are consistent with the few experimental determinations of $D^{cpx-liq}_{Fe_2O_3}$ currently available, new experiments are required to disentangle the effects of system composition and disequilibrium crystallisation on clinopyroxene-liquid Fe^{3+} partitioning. Extending our evaluation to clinopyroxene-liquid Fe^{2+}–Mg exchange equilibria suggests that $K^{cpx-liq}_{D,Fe^{2+}-Mg}$ values (as opposed to $K^{cpx-liq}_{D,Fe-Mg}$ values) lie close to experimental estimates (0.25–0.26; Sisson and Grove, 1993; Salazar-Naranjo and Vlach, 2023). Differences in apparent $K^{cpx-liq}_{D,Fe^{2+}-Mg}$ values within and between the populations of clinopyroxene crystals we analysed reflect the same disequilibrium processes recorded in ^{IV}Al-Fe^{3+} systematics, and highlight the importance of evaluating whether phases are in chemical as well as textural equilibrium before interpreting the meaning of Fe^{2+}–Mg exchange equilibria. Overall, our findings demonstrate that the non-negligible abundance of Fe^{3+} in clinopyroxene crystals from OIB settings has a significant effect on clinopyroxene-liquid Fe^{2+}–Mg exchange equilibria. While our investigation suggests that $D^{cpx-liq}_{Fe_2O_3}$ and $K^{cpx-liq}_{D,Fe^{2+}-Mg}$ values offer potential routes for estimating glass $Fe^{3+}/\Sigma Fe$ contents and ultimately magmatic f_{O_2} conditions, further experiments are required to robustly define clinopyroxene-liquid equilibria involving both Fe^{2+} and Fe^{3+}. These experiments will also pave the way for understanding equilibria between clinopyroxene and other minerals that will open new opportunities for determining and modelling the behaviour of Fe^{2+} and Fe^{3+} and thence f_{O_2} in glass-free systems.

Acknowledgements

We thank Lee Paul, David Oliver and Lewis Hughes at the University of Manchester for their help with sample preparation, thin section production and scanning electron microscopy, respectively. We also thank Stuart Kearns and Ben Buse for their help with electron probe microanalysis at the University of Bristol. We note that Rudra et al (2021) and Rudra and Hirschmann (2022) recently presented highly relevant clinopyroxene $Fe^{3+}/\Sigma Fe$ determinations by Fe-XANES. However, these articles have been retracted and can no longer form part of our discussion. We thank Luca Caricchi and Elizabeth Cottrell for their constructive comments on an earlier version of this manuscript. This work was supported by a NERC Independent Research Fellowship (NE/T011106/1) and a Royal Society Research Grant (RGS\R1\201344) to DAN.

References

Bacon CR, Druitt TH (1988) Compositional evolution of the zoned calcalkaline magma chamber of Mount Mazama, Crater Lake, Oregon. Contributions to Mineralogy and Petrology 98:224–256. https://doi.org/10.1007/BF00402114

Bali E, Hartley ME, Halldórsson SA, et al (2018) Melt inclusion constraints on volatile systematics and degassing history of the 2014–2015 Holuhraun eruption, Iceland. Contributions to Mineralogy and Petrology 173:9. https://doi.org/10.1007/s00410-017-1434-1

Berry AJ, Stewart GA, O'Neill HSC, et al (2018) A re-assessment of the oxidation state of iron in MORB glasses. Earth and Planetary Science Letters 483:114–123. https://doi.org/10.1016/j.epsl.2017.11.032

Blundy JD, Melekhova E, Ziberna L, et al (2020) Effect of redox on Fe-Mg-Mn exchange between olivine and melt and an oxybarometer for basalts. Contributions to Mineralogy and Petrology 7:103. https://doi.org/10.1007/s00410-020-01736-7

Borisov A, Behrens H, Holtz F (2018) Ferric/ferrous ratio in silicate melts: a new model for 1 atm data with special emphasis on the effects of melt composition. Contributions to Mineralogy and Petrology 173(12):98. https://doi.org/10.1007/s00410-018-1524-8

Brounce M, Stolper E, Eiler J (2017) Redox variations in Mauna Kea lavas, the oxygen fugacity of the Hawaiian plume, and the role of volcanic gases in Earth's oxygenation. Proceedings of the National Academy of Sciences 114(34):8997–9002. https://doi.org/10.1073/pnas.1619527114

Brounce M, Cottrell E, Kelley KA (2019) The redox budget of the Mariana subduction zone. Earth and Planetary Science Letters 528:115859. https://doi.org/10.1016/j.epsl.2019.115859

Brounce M, Stolper E, Eiler J (2022) The mantle source of basalts from Reunion Island is not more oxidized than the MORB source mantle. Contributions to Mineralogy and Petrology 177(1):7. https://doi.org/10.1007/s00410-021-01870-w

Burgisser A, Scaillet B (2007) Redox evolution of a degassing magma rising to the surface. Nature 445(7124):194–197. https://doi.org/10.1038/nature05509

Canil D, O'Neill HSC (1996) Distribution of Ferric Iron in some Upper-Mantle Assemblages. Journal of Petrology 37(3):609–635. https://doi.org/10.1093/petrology/37.3.609

Caricchi L, Petrelli M, Bali E, et al (2020) A Data Driven Approach to Investigate the Chemical Variability of Clinopyroxenes From the 2014–2015 Holuhraun?Bárdarbunga Eruption (Iceland). Frontiers in Earth Science

8(February):1–15. https://doi.org/10.3389/feart.2020.00018

Carmichael ISE (1991) The redox states of basic and silicic magmas: a reflection of their source regions? Contributions to Mineralogy and Petrology 106(2):129–141. https://doi.org/10.1007/BF00306429

Cottrell E, Kelley K, Lanzirotti A, et al (2009) High-precision determination of iron oxidation state in silicate glasses using XANES. Chemical Geology 268(3-4):167–179. https://doi.org/10.1016/j.chemgeo.2009.08.008

Cottrell E, Lanzirotti A, Mysen B, et al (2018) A Mössbauer-based XANES calibration for hydrous basalt glasses reveals radiation-induced oxidation of Fe. American Mineralogist 103:489–501

Cottrell E, Birner SK, Brounce M, et al (2022) Oxygen Fugacity Across Tectonic Settings. In: Moretti R, Neuville D (eds) Magma Redox Geochimistry, Geophysical Monograph 266. John Wiley & Sons, Inc., p 33–61, https://doi.org/10.1002/9781119473206.ch3

Davis FA, Cottrell E (2021) Partitioning of Fe_2O_3 in peridotite partial melting experiments over a range of oxygen fugacities elucidates ferric iron systematics in mid-ocean ridge basalts and ferric iron content of the upper mantle. Contributions to Mineralogy and Petrology 176(9):67. https://doi.org/10.1007/s00410-021-01823-3

Downes MJ (1974) Sector and oscillatory zoning in calcic augites from M. Etna, Sicily. Contributions to Mineralogy and Petrology 47(3):187–196. https://doi.org/10.1007/BF00371538

Dowty E (1976) Crystal structure and crystal growth: II. sector zoning in minerals. American Mineralogist 61:460–469

Droop GTR (1987) A general equation for Estimating Fe^{3+} concentrations in ferromagnesian silicates and oxides from microprobe analyses, using stoichiometric criteria. Mineralogical Magazine 51(361):431–435. https://doi.org/10.1180/minmag.1987.051.361.10

Dyar MD, Gunter ME, Delany JS, et al (2002) Systematics in the structure and XANES spectra of pyroxenes, amphiboles, and micas as derived from oriented single crystals. Canadian Mineralogist 40(5):1375–1393. https://doi.org/10.2113/gscanmin.40.5.1375

Evans KA (2006) Redox decoupling and redox budgets: Conceptual tools for the study of earth systems. Geology 34(6):489–492. https://doi.org/10.1130/G22390.1

Evans KA, Tomkins AG (2011) The relationship between subduction zone redox budget and arc magma fertility. Earth and Planetary Science Letters 308(3-4):401–409. https://doi.org/10.1016/j.epsl.2011.06.009

Evans KA, Tomkins AG (2022) Redox Variables and Mechanisms in Subduction Magmatism and Volcanism. In: Moretti R, Neuville DR (eds) Geophysical Monograph Series, 1st edn. Wiley, p 63–91, https://doi.org/10.1002/9781119473206.ch4

Feig ST, Koepke J, Snow JE (2010) Effect of oxygen fugacity and water on phase equilibria of a hydrous tholeiitic basalt. Contributions to Mineralogy and Petrology 160(4):551–568. https://doi.org/10.1007/s00410-010-0493-3

Fran ca ZT, Tassinari CC, Cruz JV, et al (2006) Petrology, geochemistry and Sr?Nd?Pb isotopes of the volcanic rocks from Pico Island–Azores (Portugal). Journal of Volcanology and Geothermal Research 156(1-2):71–89. https://doi.org/10.1016/j.jvolgeores.2006.03.013

Frost BR (1991) Introduction to oxygen fugacity and its petrologic importance. Reviews in Mineralogy and Geochemistry 25:1–9

Gaetani GA (2016) The Behavior of $Fe^{3+}/\Sigma Fe$ During Partial Melting of Spinel Lherzolite. Geochimica et Cosmochimica Acta 185:64–77. https://doi.org/10.1016/j.gca.2016.03.019

Gaillard F, Scaillet B, Arndt NT (2011) Atmospheric oxygenation caused by a change in volcanic degassing pressure. Nature 478(7368):229–232. https://doi.org/10.1038/nature10460

van Gerve TD, Neave DA, Wieser P, et al (2024) The origin and differentiation of CO_2-rich primary melts in Ocean Island volcanoes: Integrating 3D X-ray tomography with chemical microanalysis of olivine-hosted melt inclusions from Pico (Azores). Journal of Petrology egae006. https://doi.org/10.1093/petrology/egae006,

Ghiorso MS, Evans BW (2008) Thermodynamics of rhombohedral oxide solid solutions and a revision of the Fe-Ti two-oxide geothermometer and oxygen-barometer. American Journal of Science 308(9):957–1039. https://doi.org/10.2475/09.2008.01

Ghiorso MS, Sack RO (1995) Chemical mass transfer in magmatic processes IV. A revised and internally consistent thermodynamic model for the interpolation and extrapolation of liquid-solid equilibria in magmatic systems at elevated temperatures and pressures. Contributions to Mineralogy and Petrology 119(2-3):197–212. https://doi.org/10.1007/BF00307281

Halldórsson SA, Bali E, Hartley ME, et al (2018) Petrology and geochemistry of the 2014–2015 Holuhraun eruption, central Iceland: compositional and mineralogical characteristics, temporal variability and magma storage. Contributions to Mineralogy and Petrology 173:64. https://doi.org/10.1007/s00410-018-1487-9

Hartley ME, Shorttle O, Maclennan J, et al (2017) Olivine-hosted melt inclusions as an archive of redox heterogeneity in magmatic systems. Earth and Planetary Science Letters 479:192–205. https://doi.org/10.1016/j.epsl.2017.09.029

Helz RT, Cottrell E, Brounce MN, et al (2017) Olivine-Melt Relationships and Syneruptive Redox Variations in the 1959 Eruption of Kīlauea Volcano as Revealed by XANES. Journal of Volcanology and Geothermal Research 333-334:1–14. https://doi.org/10.1016/j.jvolgeores.2016.12.006

Holland HD (2002) Volcanic gases, black smokers, and the great oxidation event. Geochimica et Cosmochimica Acta 66(21):3811–3826. https://doi.org/10.1016/S0016-7037(02)00950-X

Holland TJB, Powell R (1998) An internally consistent thermodynamic data set for phases of petrological interest. Journal of Metamorphic Geology 16(3):309–343. https://doi.org/10.1111/j.1525-1314.1998.00140.x

Holland TJB, Green ECR, Powell R (2018) Melting of peridotites through to granites: a simple thermodynamic model in the system KNCFMASHTOCr. Journal of Petrology 59(5):881–900. https://doi.org/10.1093/petrology/egy048

Hughes EC, Saper L, Liggins P, et al (2023) The sulfur solubility minimum and maximum in silicate melt. Journal of the Geological Society pp 1–50. https://doi.org/10.1144/jgs2021-125

Jennings ES, Holland TJB (2015) A simple thermodynamic model for melting of peridotite in the system NCFMASOCr. Journal of Petrology pp 1–24. https://doi.org/10.1093/petrology/egv020

Jochum KP, Willbold M, Raczek I, et al (2005) Chemical characterisation of the USGS reference glasses GSA-1G, GSC-1G, GSD-1G, GSE-1G, BCR-2G, BHVO-2G and BIR-1G using EPMA, ID-TIMS, ID-ICP-MS and LA-ICP-MS. Geostandards and Geoanalytical Research 29:285–302

Jugo PJ (2009) Sulfur content at sulfide saturation in oxidized magmas. Geology 37(5):415–418. https://doi.org/10.1130/G25527A.1

Kelley KA, Cottrell E (2009) Water and the Oxidation State of Subduction Zone Magmas. Science 325(5940):605–607. https://doi.org/10.1126/science.1174156

Kouchi A, Sugawara Y, Kashima K, et al (1983) Laboratory growth of sector zones clinopyroxenes in the system $CaMgSi_2O_6$ – $CaTiAl_2O_6$. Contributions to Mineralogy and Petrology 83:177–184

Kress VC, Carmichael ISE (1991) The compressibility of silicate liquids containing Fe_2O_3 and the effect of composition, temperature, oxygen fugacity and pressure on their redox states. Contributions to Mineralogy and Petrology 108(1-2):82–92. https://doi.org/10.1007/BF00307328

Larsen LM (1976) Clinopyroxenes and Coexisting Mafic Minerals from the Alkaline Ilimaussaq Intrusion, South Greenland. Journal of Petrology 17(2):258–290. https:

//doi.org/10.1093/petrology/17.2.258

Lee CTA, Leeman WP, Canil D, et al (2005) Similar V/Sc systematics in MORB and arc basalts: Implications for the oxygen fugacities of their mantle source regions. Journal of Petrology 46(11):2313–2336. https://doi.org/10.1093/petrology/egi056, iSBN: 0022-3530\r1460-2415

Lee CTA, Luffi P, Chin EJ, et al (2012) Copper Systematics in Arc Magmas and Implications for Crust-Mantle Differentiation. Science 336(6077):64–68. https://doi.org/10.1126/science.1217313

Leung IS (1974) Sector-zoned Titanaugites: Morphology, Crystal Chemistry, and Growth. American Mineralogist 59:127–138

Lindsley DH (1983) Pyroxene thermometry. American Mineralogist 68(5-6):477–493. https://doi.org/10.1007/BF00372872

Lindsley DH, Andersen DJ (1983) A two-pyroxene thermometer. Journal of Geophysical Research 88 Supplem:A887–A906. https://doi.org/10.1029/JB088iS02p0A887

Loughlin SC (1995) The evolution of the Eyjafjöll volcanic system, southern Iceland. PhD, Durham University, Durham

Luth RW, Canil D (1993) Ferric iron in mantle-derived pyroxenes and a new oxybarometer for the mantle. Contributions to Mineralogy and Petrology 113(2):236–248. https://doi.org/10.1007/BF00283231

Mallmann G, O'Neill HSC (2009) The crystal/melt partitioning of V during mantle melting as a function of oxygen fugacity compared with some other elements (Al, P, Ca, Sc, Ti, Cr, Fe, Ga, Y, Zr and Nb). Journal of Petrology 50(9):1765–1794. https://doi.org/10.1093/petrology/egp053

McCammon C (2021) Mössbauer Spectroscopy with High Spatial Resolution: Spotlight on Geoscience. In: Yoshida Y, Langouche G (eds) Modern Mössbauer Spectroscopy, vol 137. Springer Singapore, Singapore, p 221–266, https://doi.org/10.1007/978-981-15-9422-9_5

McCanta MC, Dyar MD, Rutherford MJ, et al (2004) Iron partitioning between basaltic melts and clinopyroxene as a function of oxygen fugacity. American Mineralogist 89(11-12):1685–1693. https://doi.org/10.2138/am-2004-11-1214, iSBN: 0003-004X

McGuire AV, Dyar MD, Ward KA (1989) Neglected Fe^{3+}/Fe^{2+} ratios – a study of Fe^{3+} content of megacrysts from alkali basalts. Geology 17(8):687–690. https://doi.org/10.1130/0091-7613(1989)017<0687:NFFRAS>2.3.CO

Mollo S, Del Gaudio P, Ventura G, et al (2010) Dependence of clinopyroxene composition on cooling rate in basaltic magmas: Implications for thermobarometry. Lithos 118(3-4):302–312. https://doi.org/10.1016/j.lithos.2010.05.006

Mollo S, Putirka KD, Misiti V, et al (2013) A new test for equilibrium based on clinopyroxene-melt pairs: Clues on the solidification temperatures of Etnean alkaline melts at post-eruptive conditions. Chemical Geology 352:92–100. https://doi.org/10.1016/j.chemgeo.2013.05.026

Mollo S, Blundy JD, Scarlato P, et al (2018) An integrated P-T-H_2O-lattice strain model to quantify the role of clinopyroxene fractionation on REE+Y/HFSE patterns of mafic alkaline magmas: Application to eruptions at Mt. Etna. Earth-Science Reviews 185:32–56. https://doi.org/10.1016/j.earscirev.2018.05.014

Morimoto N, Fabries J, Ferguson AK, et al (1988) Nomenclature of pyroxenes. American Mineralogist 73:1123–1133. https://doi.org/10.1007/BF01226262

Moussallam Y, Oppenheimer C, Scaillet B, et al (2014) Tracking the changing oxidation state of Erebus magmas, from mantle to surface, driven by magma ascent and degassing. Earth and Planetary Science Letters 393:200–209. https://doi.org/10.1016/j.epsl.2014.02.055

Moussallam Y, Edmonds M, Scaillet B, et al (2016) The impact of degassing on the oxidation state of basaltic magmas: A case study of Kīlauea volcano. Earth and Planetary Science Letters 450:317–325. https://doi.org/10.1016/j.epsl.2016.06.031

Moussallam Y, Longpré MA, McCammon CA, et al (2019) Mantle plumes are oxidised. Earth and Planetary Science Letters 527:115798. https://doi.org/10.1016/j.epsl.2019.115798

Musu A, Corsaro RA, Higgins O, et al (2023) The magmatic evolution of South-East Crater (Mt. Etna) during the February–April 2021 sequence of lava fountains from a mineral chemistry perspective. Bulletin of Volcanology 85(5):33. https://doi.org/10.1007/s00445-023-01643-2

Muth MJ, Cottrell E (2023) No detectable redox exchange between sulfur and iron during rapid cooling of basalts. Earth and Planetary Science Letters 616:118210. https://doi.org/10.1016/j.epsl.2023.118210

Neave D, Stewart A, Hartley M, et al (2024) Re-evaluating stoichiometric estimates of iron valence in magmatic clinopyroxene crystals. Contributions to Mineralogy and Petrology 179(5):17. https://doi.org/10.1007/s00410-023-02080-2

Neave DA, Maclennan J (2020) Clinopyroxene Dissolution Records Rapid Magma Ascent. Frontiers in Earth Science 8:188. https://doi.org/10.3389/feart.2020.00188

Neave DA, Putirka KD (2017) A new clinopyroxene-liquid barometer, and implications for magma storage pressures under Icelandic rift zones. American Mineralogist 102:777–794. https://doi.org/10.2138/am-2017-5968

Neave DA, Passmore E, Maclennan J, et al (2013) Crystal-melt relationships and the record of deep mixing and crystallization in the AD 1783 Laki eruption, Iceland. Journal of Petrology 54(8):1661–1690. https://doi.org/10.1093/petrology/egt027

Neave DA, Maclennan J, Hartley ME, et al (2014) Crystal storage and transfer in basaltic systems: the Skuggafjöll eruption, Iceland. Journal of Petrology 55(12):2311–2346. https://doi.org/10.1093/petrology/egu058

Neave DA, Bali E, Guðfinnsson GH, et al (2019) Clinopyroxene-liquid equilibria and geothermobarometry in natural and experimental tholeiites: the 2014–2015 Holuhraun eruption, Iceland. Journal of Petrology 60:1653–1680. https://doi.org/10.1093/petrology/egz042

Nicklas R, Hahn R, Day J (2022a) Oxidation of La Réunion lavas with MORB-like fO2 by assimilation. Geochemical Perspectives Letters 20:32–36. https://doi.org/10.7185/geochemlet.2205

Nicklas RW, Hahn RK, Willhite LN, et al (2022b) Oxidized mantle sources of HIMU- and EM-type Ocean Island Basalts. Chemical Geology 602:120901. https://doi.org/10.1016/j.chemgeo.2022.120901

Nikkola P, Bali E, Kahl M, et al (2019) Mid-crustal storage and crystallization of Eyjafjallajökull. Jökull 69:77–96

O'Neill HSC (2021) The Thermodynamic Controls on Sulfide Saturation in Silicate Melts with Application to Ocean Floor Basalts. In: Neuville DR, Moretti R (eds) Magma Redox Geochemistry, Geophysical Monograph 266. American Geophysical Union, Washington D.C., p 177–213, https://doi.org/10.1002/9781119473206.ch10

O'Neill HSC, Berry AJ, Mallmann G (2018) The oxidation state of iron in Mid-Ocean Ridge Basaltic (MORB) glasses: Implications for their petrogenesis and oxygen fugacities. Earth and Planetary Science Letters 504:152–162. https://doi.org/10.1016/j.epsl.2018.10.002

Oppenheimer C, Moretti R, Kyle PR, et al (2011) Mantle to surface degassing of alkalic magmas at Erebus volcano, Antarctica. Earth and Planetary Science Letters 306(3-4):261–271. https://doi.org/10.1016/j.epsl.2011.04.005

Passmore E, Maclennan J, Fitton JG, et al (2012) Mush disaggregation in basaltic magma chambers: Evidence from the AD 1783 Laki eruption. Journal of Petrology 53(12):2593–2623. https://doi.org/10.1093/petrology/egs061

Powell R, Holland TJB, Worley N (1998) Calculating phase diagrams involving solid solutions via non-linear equations, with examples using THERMOCALC. Journal of Metamorphic Geology 16:577–588. https://doi.org/10.1111/j.1525-1314.1998.00157.x

Putirka KD (2008) Thermometers and Barometers for Volcanic Systems. Reviews in Mineralogy and Geochemistry 69(1):61–120. https://doi.org/10.2138/rmg.2008.69.3

Putirka KD, Johnson M, Kinzler RJ, et al (1996) Thermobarometry of mafic igneous rocks based on clinopyroxene-liquid equilibria, 0?30 kbar. Contributions to Mineralogy and Petrology 123(1):92–108. https://doi.org/10.1007/s004100050145

Reay A, Johnstone R, Kawachi Y (1989) Kaersutite, a possible international microprobe standard. Geostandards and Geoanalytical Research 13(1):187–190. https://doi.org/10.1111/j.1751-908X.1989.tb00471.x

Riel N, Kaus BJP, Green ECR, et al (2022) MAGEMin, an Efficient Gibbs Energy Minimizer: Application to Igneous Systems. Geochemistry, Geophysics, Geosystems 23(7):1–27. https://doi.org/10.1029/2022GC010427

Robinson P (1980) The composition space of terrestrial pyroxenes -internal and external limits. Reviews in Mineralogy and Geochemistry 7:419–494. https://doi.org/10.1515/9781501508257-013

Roeder PL, Emslie RF (1970) Olivine-liquid equilibrium. Contributions to Mineralogy and Petrology 29(4):275–289. https://doi.org/10.1007/BF00371276

Rudra A, Hirschmann MM (2022) Fe3+ partitioning between clinopyroxene and silicate melt at 1–2.5 GPa: implications for Fe^{3+} content of MORB and OIB source mantle. Geochimica et Cosmochimica Acta 328:258–279. https://doi.org/10.1016/j.gca.2022.04.023

Rudra A, Cottrell E, Hirschmann MM (2021) Experimental determination of ferric iron partitioning between pyroxene and melt at 100 kPa. Chemical Geology 584:120532. https://doi.org/10.1016/j.chemgeo.2021.120532

Sack RO, Ghiorso MS (1994) Thermodynamics of multicomponent pyroxenes: III. Calibration of $Fe^{2+}(Mg)_{-1}$, $TiAl_2(MgSi_2)_{-1}$, $TiFe^{3+}{}_{,2}(MgSi_2)_{-1}$, $AlFe^{3+}(MgSi)_{-1}$, $NaAl(CaMg)_{-1}$, $Al_2(MgSi)_{-1}$ and $Ca(Mg)_{-1}$ exchange reactions between pyroxenes and silicate melts. Contributions to Mineralogy and Petrology 118(3):271–296. https://doi.org/10.1007/BF00306648

Salazar-Naranjo AF, Vlach SRF (2023) New experimental constraints for the evolution and thermobarometry of alkali ultrabasic to intermediate igneous rocks. Journal of Petrology 64(11):egad078. https://doi.org/10.1093/petrology/egad078

Saper LM, Stolper MB, Baker EM (2022) Fe^{2+}–Mg partitioning between olivine and liquid at low oxygen fugacity: an experimental and thermodynamic framework. Contributions to Mineralogy and Petrology 177:94. https://doi.org/10.1007/s00410-022-01955-0

Shorttle O (2015) Geochemical variability in MORB controlled by concurrent mixing and crystallisation. Earth and Planetary Science Letters 424:1–14. https://doi.org/10.1016/j.epsl.2015.04.035

Sisson TW, Grove TL (1993) Experimental investigations of the role of H_2O in calc-alkaline differentiation and subduction zone magmatism. Contributions to Mineralogy and Petrology 113(2):143–166. https://doi.org/10.1007/BF00283225

Steven CJ, Dyar MD, McCanta M, et al (2022) The absorption indicatrix as an empirical model to describe anisotropy in X-ray absorption spectra of pyroxenes. American Mineralogist 107(4):654–663. https://doi.org/10.2138/am-2021-7950

Stracke A (2012) Earth's heterogeneous mantle: A product of convection-driven interaction between crust and mantle. Chemical Geology 330-331:274–299. https://doi.org/10.1016/j.chemgeo.2012.08.007

Taracsák Z, Longpré MA, Tartèse R, et al (2022) Highly oxidising conditions in volatile-rich El Hierro magmas: implications for ocean island magmatism. Journal of Petrology 63:1–21. https://doi.org/10.1093/petrology/egac011

Thomson A, Maclennan J (2013) The distribution of olivine compositions in Icelandic basalts and picrites. Journal of Petrology 54(4):745–768. https://doi.org/10.1093/petrology/egs083

Toplis MJ, Carroll MR (1995) An Experimental Study of the Influence of Oxygen Fugacity on Fe-Ti Oxide Stability, Phase Relations, and Mineral-Melt Equilibria in Ferro-Basaltic Systems. Journal of Petrology 36(5):1137–1170. URL http://petrology.oxfordjournals.org/content/36/5/1137.abstract

Ubide T, Mollo S, Zhao JX, et al (2019) Sector-zoned clinopyroxene as a recorder of magma history, eruption triggers, and ascent rates. Geochimica et Cosmochimica Acta 251:265–283. https://doi.org/10.1016/j.gca.2019.02.021

Ulmer P, Kägi R, Müntener O (2018) Experimentally derived intermediate to silica-rich arc magmas by fractional and equilibrium crystallization at 1.0 GPa: An evaluation of phase relationships, compositions, liquid lines of descent and oxygen fugacity. Journal of Petrology 59:11–58. https://doi.org/10.1093/petrology/egy017/4866144

Weis D, Harpp KS, Harrison LN, et al (2023) Earth's mantle composition revealed by mantle plumes. Nature Reviews Earth & Environment https://doi.org/10.1038/s43017-023-00467-0, URL https://www.nature.com/articles/s43017-023-00467-0

Weis FA, Skogby H, Troll VR, et al (2015) Magmatic water contents determined through clinopyroxene: Examples from the Western Canary Islands, Spain. Geochemistry, Geophysics, Geosystems 16:2127–2146. https://doi.org/10.1002/2015GC005800

White JC, Ren M, Parker DF (2005) Variation in mineralogy, temperature, and oxygen fugacity in a suite of strongly peralkaline lavas and tuffs, Pantelleria, Italy. Canadian Mineralogist 43(4):1331–1347. https://doi.org/10.2113/gscanmin.43.4.1331

Wieser PE, Kent AJR, Till CB (2023a) Barometers Behaving Badly II: a Critical Evaluation of Cpx–Only and Cpx-Liq Thermobarometry in Variably-Hydrous Arc Magmas. Journal of Petrology 64(8):egad050. https://doi.org/10.1093/petrology/egad050

Wieser PE, Kent AJR, Till CB, et al (2023b) Barometers Behaving Badly I: Assessing the Influence of Analytical and Experimental Uncertainty on Clinopyroxene Thermobarometry Calculations at Crustal Conditions. Journal of Petrology 64(2):1–27. https://doi.org/10.1093/petrology/egac126

Wood BJ, Blundy JD (1997) A predictive model for rare earth element partitioning between clinopyroxene and anhydrous silicate melt. Contributions to Mineralogy and Petrology 129(2-3):166–181. https://doi.org/10.1007/s004100050330

Wood BJ, Bryndzia LT, Johnson KE (1990) Mantle oxidation state and its relationship to tectonic environment and fluid speciation. Science 248(4953):337

Zanon V, Pimentel A, Auxerre M, et al (2020) Unravelling the magma feeding system of a young basaltic oceanic volcano. Lithos 352-353:105325. https://doi.org/10.1016/j.lithos.2019.105325

Zindler A, Hart SR (1986) Chemical Geodynamics. Annual Reviews of Earth and Planetary Sciences 14(1):493–571. https://doi.org/10.1146/annurev.earth.14.1.493

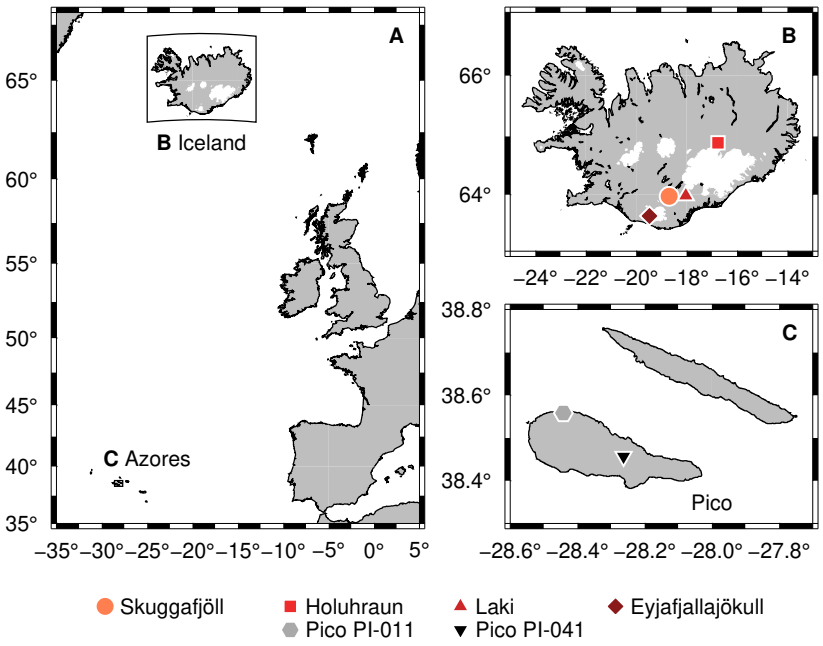

Figure 1: (A) Map of the North Atlantic encompassing sample locations in Iceland and the Azores. (B) Map of Iceland showing the location of samples from Skuggafjöll, Holuhraun, Laki and Eyjafjallajökull.(C) Map of part of the Azores archipelago showing the location of samples on Pico Island.

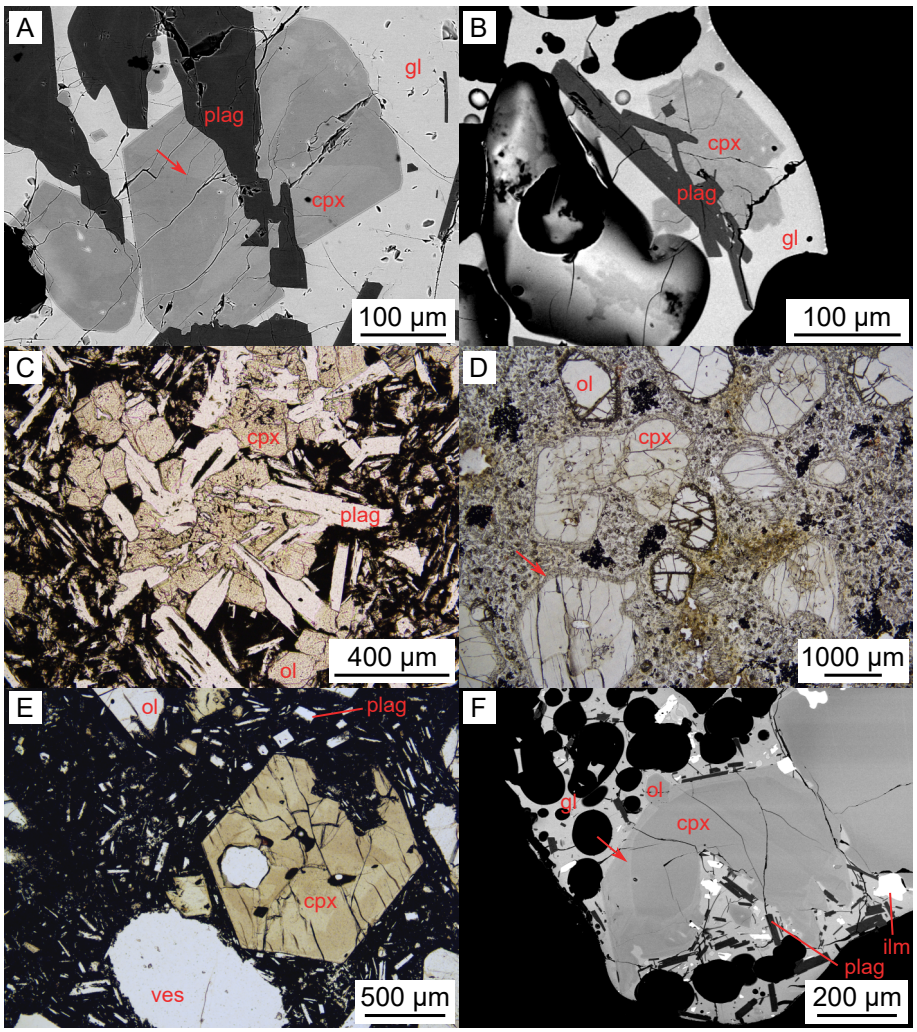

Figure 2: Clinopyroxene textures in ocean island basalt samples from Iceland and the Azores. Labels are as follows: cpx, clinopyroxene; ol, olivine; plag, plagioclase; gl, glass; ilm, ilmenite; and ves, vesicle. (A) Backscattered electron (BSE) image of clinopyroxene in pillow basalt HOR-11-01 from Skuggafjöll. An interface between high-BSE-intensity $\{hk0\}$ prism sectors and low-BSE-intensity $\{\bar{1}11\}$ hourglass sectors is highlighted with an arrow. (B) BSE image of ophitic clinopyroxene in a basaltic tephra sample from Holuhraun. (C) Photomicrograph of clinopyroxene in ophitic arrangement in basaltic lava sample LAK-04 from Laki. (D) Photomicrograph of large clinopyroxene macrocrysts in ankaramitic lava sample HVAM13-01 from Eyjafjallajökull. The arrow shows rims undergoing dissolution (Neave and Maclennan, 2020). (E) Photomicrograph of a large clinopyroxene macrocrysts in basaltic lava sample PI-011 from Pico, Azores. Sector zoning is reflected in the variable colour of the clinopyroxene macrocryst. (F) BSE image of large clinopyroxene macrocysts in basaltic tephra sample PI-041 from Pico, Azores. A prominent concentric zoning boundary is highlighted with the arrow.

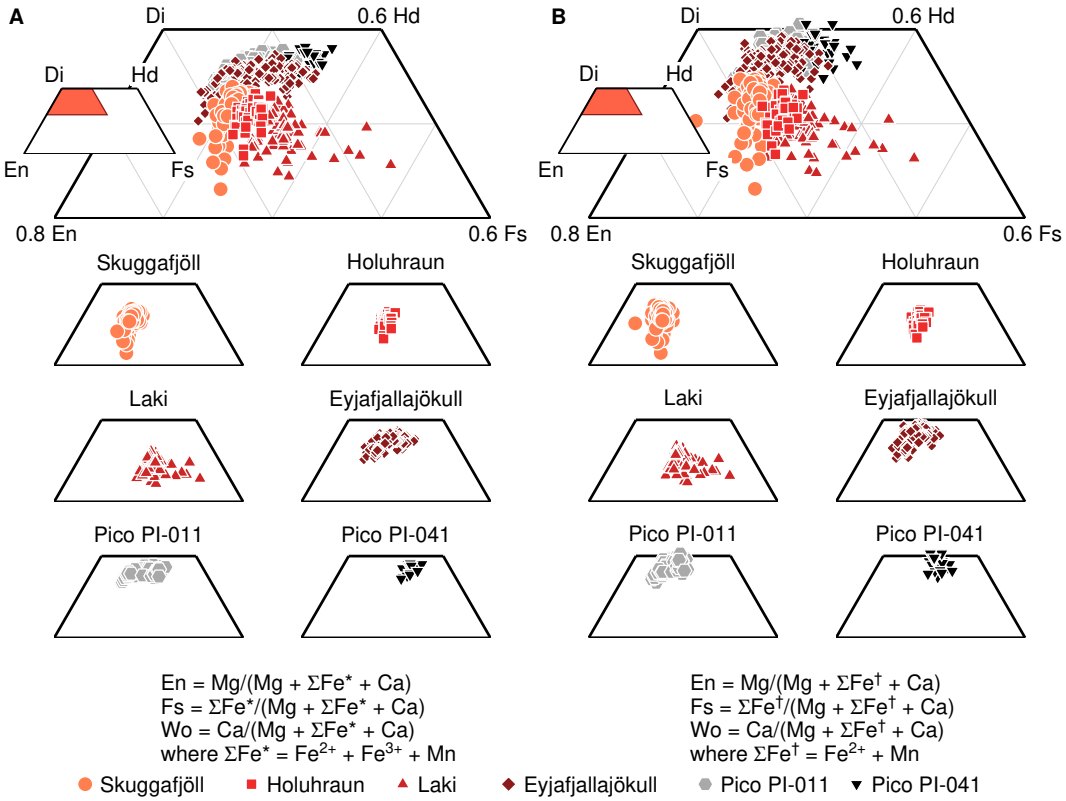

Figure 3: Summary of clinopyroxene compositions in ocean island basalt samples from Iceland and the Azores. (A) Pyroxene quadrilateral showing clinopyroxene quadrilateral components (diopside, Di; hedenbergite, Hd; enstatite, En; and ferrosilite, Fs) calculated following Morimoto et al (1988) where the Fe component (ΣFe*) is equal to the sum of Fe^{2+}, Fe^{3+} and Mn. (B) Pyroxene quadrilateral showing adjusted clinopyroxene quadrilateral components (diopside, $Di^{\dagger}$; hedenbergite, $Hd^{\dagger}$; enstatite, $En^{\dagger}$; and ferrosilite, $Fs^{\dagger}$) calculated following Morimoto et al (1988) where the Fe component ($\Sigma Fe^{\dagger}$) is equal to the sum of Fe^{2+} and Mn, with Fe^{2+} determined by stoichiometry following Droop (1987).

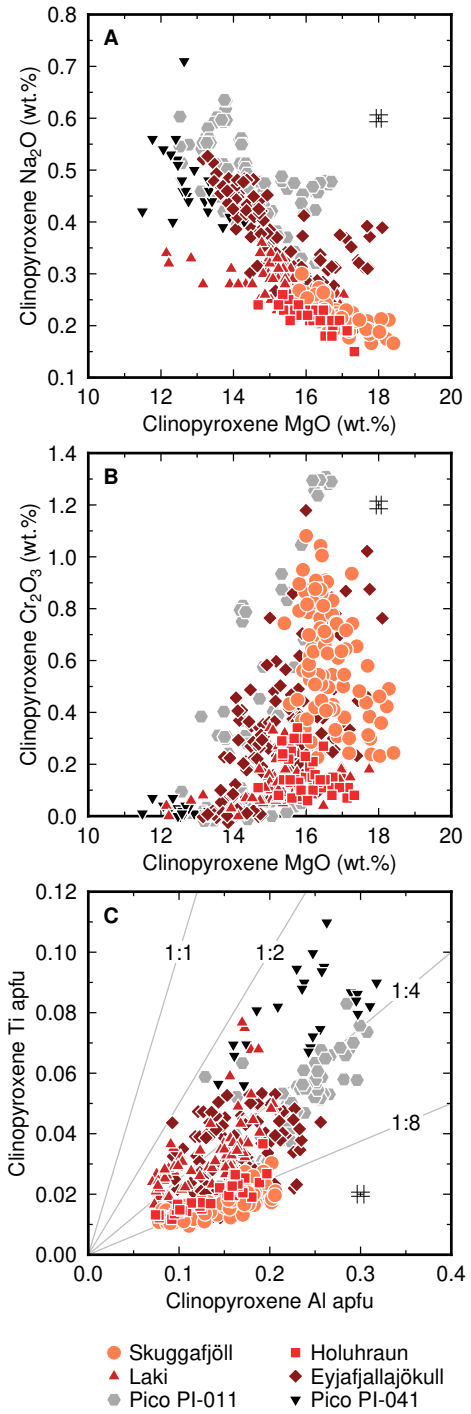

Figure 4: Systematics of major elements hosted in non-quadrilateral clinopyroxene components in ocean island samples from Iceland and the Azores; 1σ analytical uncertainties are shown. (A) Variation in Na_2O as a function of MgO. (B) Variation in Cr_2O_3 as a function of MgO. (C) Covariation of Ti and Al atoms per formula unit (apfu) calculated on a six-oxygen basis.

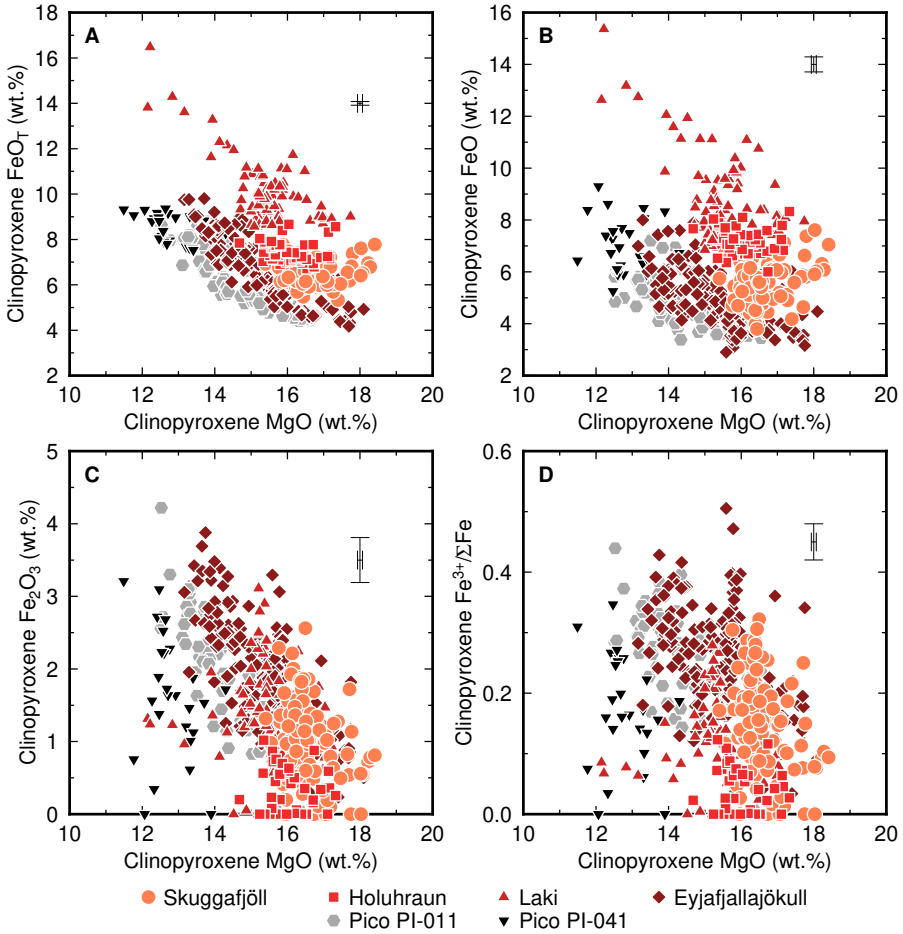

Figure 5: Iron concentration and valence systematics in clinopyroxene crystals from Iceland and the Azores; 1σ analytical uncertainties are shown. (A) MgO versus total Fe expressed as FeO (FeO_T). (B) MgO versus FeO determined by stoichiometry following Droop (1987). (C) MgO versus Fe_2O_3 determined by stoichiometry following Droop (1987). (D) MgO versus $Fe^{3+}/\Sigma Fe$ determined by stoichiometry following Droop (1987).

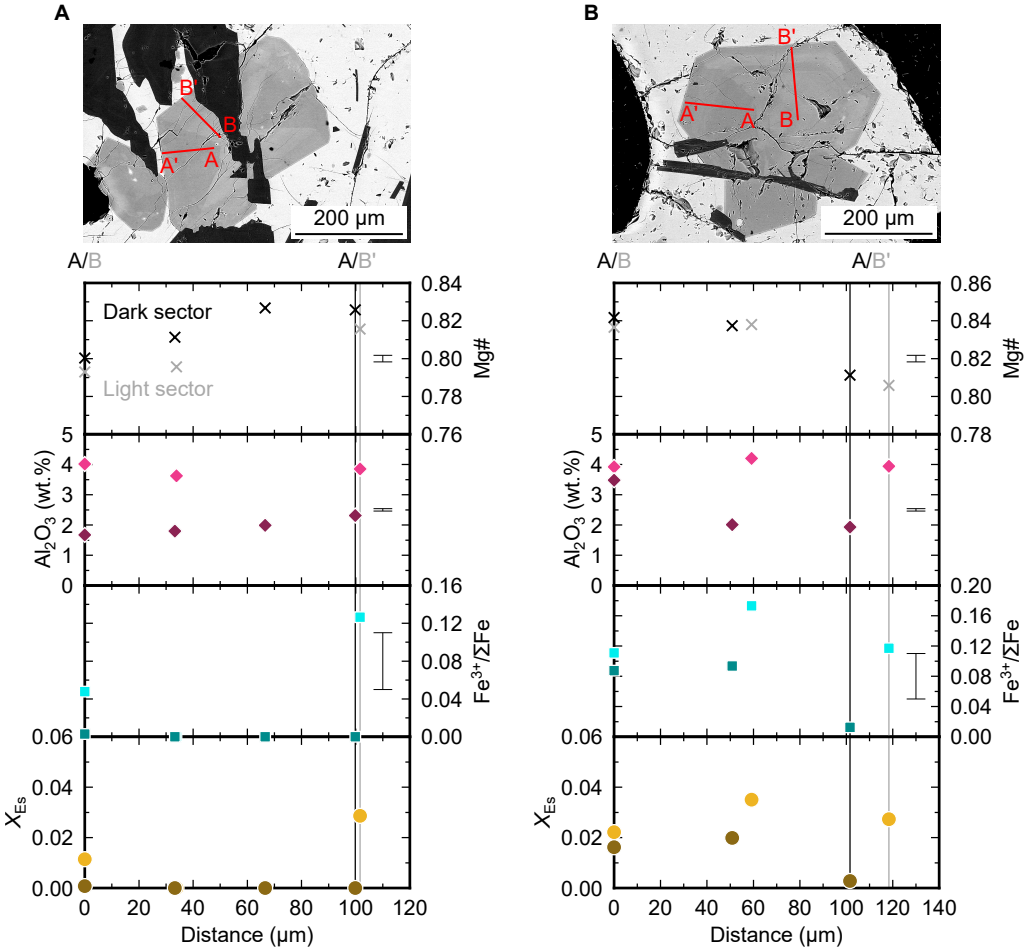

Figure 6: Chemical systematics of clinopyroxene crystals with hourglass sector zoning in samples from Skuggafjöll, Iceland. Light and dark symbols show core-to-rim profiles from high- and low-backscattered electron (BSE)-intensity zones, respectively; 1σ analytical uncertainties are shown. Vertical lines show the positions of crystal rims. High-BSE-intensity zones are richer in Al_2O_3, Fe^{3+} and esseneite (Es, $CaFe^{3+}AlSiO_6$) component than low-BSE-intensity zones.

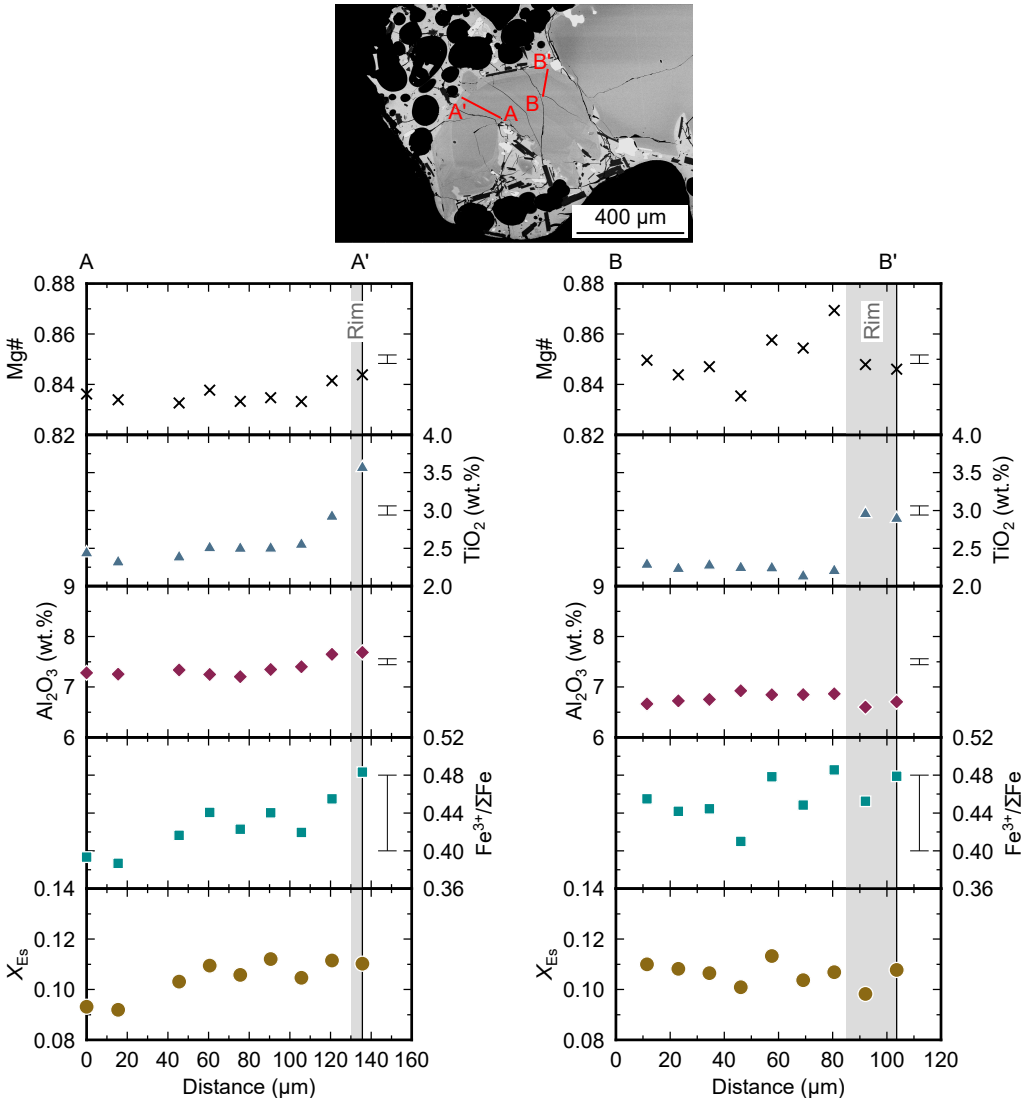

Figure 7: Chemical systematics of clinopyroxene crystals with concentric core-to-rim zoning in samples from Pico (PI-041), Azores. Vertical lines show the positions of crystal rims and grey shading shows the extent of rim zones identified from backscattered electron (BSE) images; 1σ analytical uncertainties are shown. Rims are primarily reflected in changes in Mg# and TiO_2 content rather than systematic changes in $Fe^{3+}/\Sigma Fe$ and esseneite (Es, $CaFe^{3+}AlSiO_6$) component.

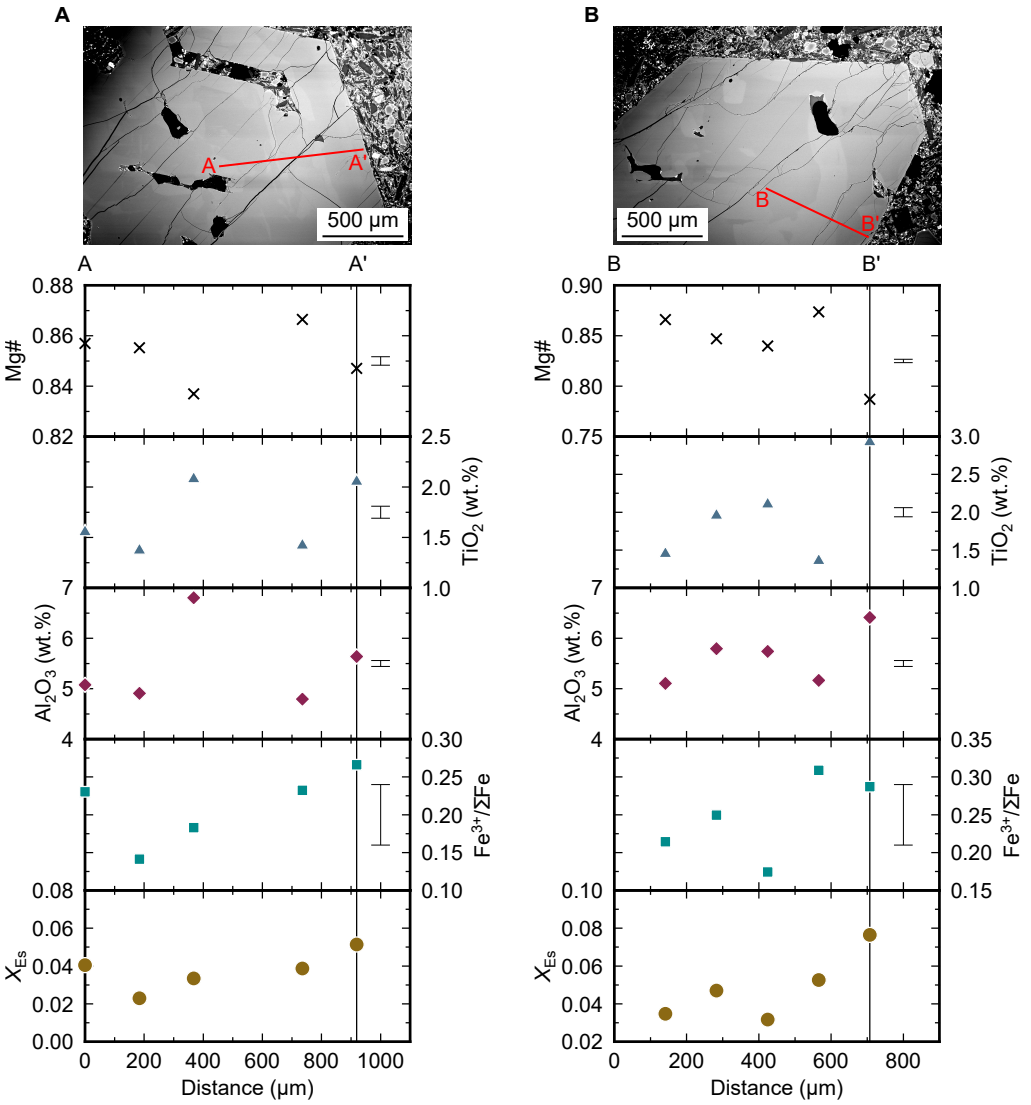

Figure 8: Chemical systematics of clinopyroxene crystals with patchy sector zoning in samples from Pico (PI-011), Azores. Vertical lines show the positions of crystal rims; 1σ analytical uncertainties are shown. There is considerable variability in Mg#, TiO_2, $Fe^{3+}/\Sigma Fe$ and esseneite (Es, $CaFe^{3+}AlSiO_6$) component contents in crystals with patchy sector zoning but this variability is less systematic than that observed in crystals with hourglass sector zoning or concentric core-to-rim zoning (Figures 6 and 7).

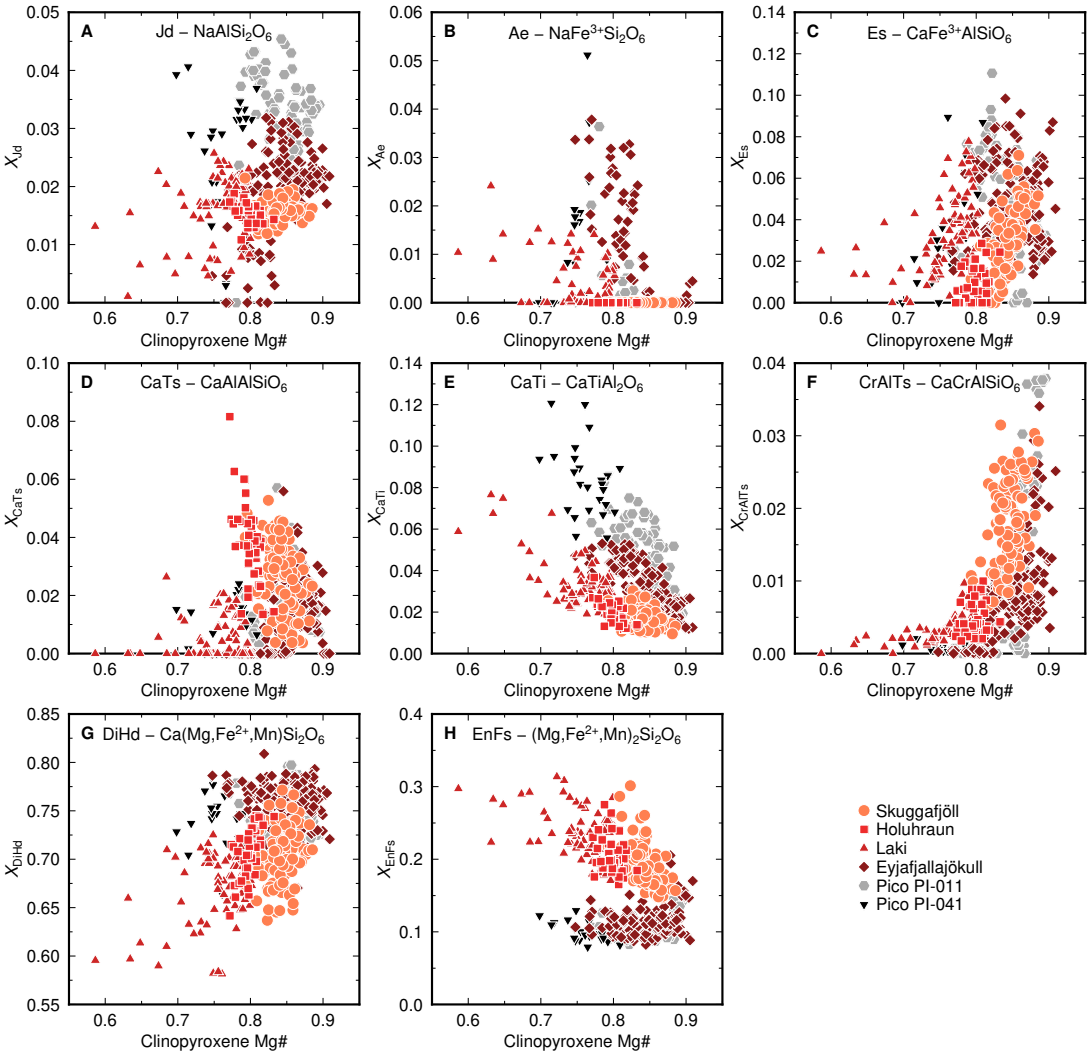

Figure 9: Clinopyroxene components in ocean island samples from Iceland and the Azores summarised as functions of clinopyroxene Mg#, where Mg# = molar $Mg/(Mg+Fe^{2+})$. The scheme for calculating the following components was described by Neave et al (2024) and is summarised in the appendix. (A) jadeite, Jd; (B) aegirine, Ae; (C) esseneite, Es; (D) calcium-Tschermak's component, CaTs; (E) titanian calcium-Tschermak's component, CaTi; (F) chromian calcium-Tschermak's component, CrCaTs; (G) diopside and hedenbergite, DiHd; and (H) enstatite and ferrosilite, EnFs.

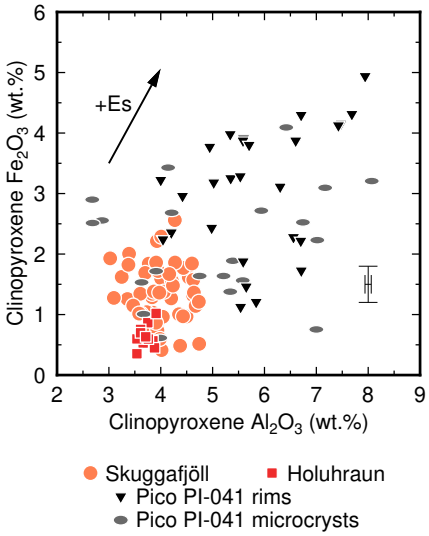

Figure 10: Variations in clinopyroxene Al_2O_3 and Fe_2O_3 contents in samples from Skuggaföll, Holuhraun and Pico (PI-041) that are textural in equilibrium with their host glasses. Although analyses in PI-041 and our samples from Skuggafjöll are more variable than those in our Holuhraun sample, much of the coupled variability across these samples can be explained by incorporating variable amounts of esseneite (Es, $CaFe^{3+}AlSiO_6$) component, as illustrated by the vector labelled +Es.

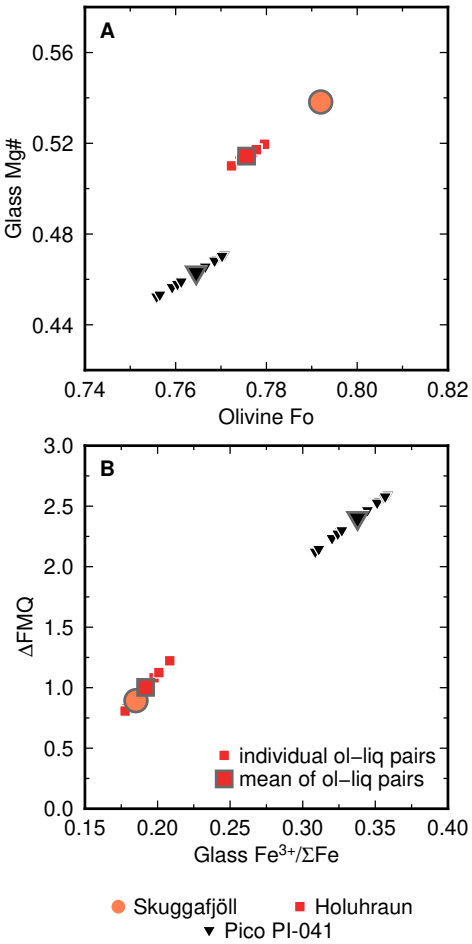

Figure 11: Estimating pre-eruptive magmatic oxygen fugacity (f_{O_2}) conditions recorded by olivine-liquid equilibria in samples from Skuggaföll, Holuhraun and Pico (PI-041). (A) Estimation of glass Mg# contents, where Mg# = Mg/(Mg+Fe^{2+}). Glass Fe^{2+} contents were estimated using the $K^{ol-liq}_{D,Fe^{2+}-Mg}$ model of Saper et al (2022) that assumes all Fe occurs as Fe^{2+}. Equilibrium olivine-liquid pairs were identified texturally from BSE images. (B) Conversion of estimated glass $Fe^{3+}/\Sigma Fe$ contents into f_{O_2} conditions (expressed as log units relative to fayalite-magnetite-quartz equilibrium; ΔFMQ) according to the model of Borisov et al (2018). Large symbols show mean values that reflect our best estimates of magmatic (f_{O_2}) conditions.

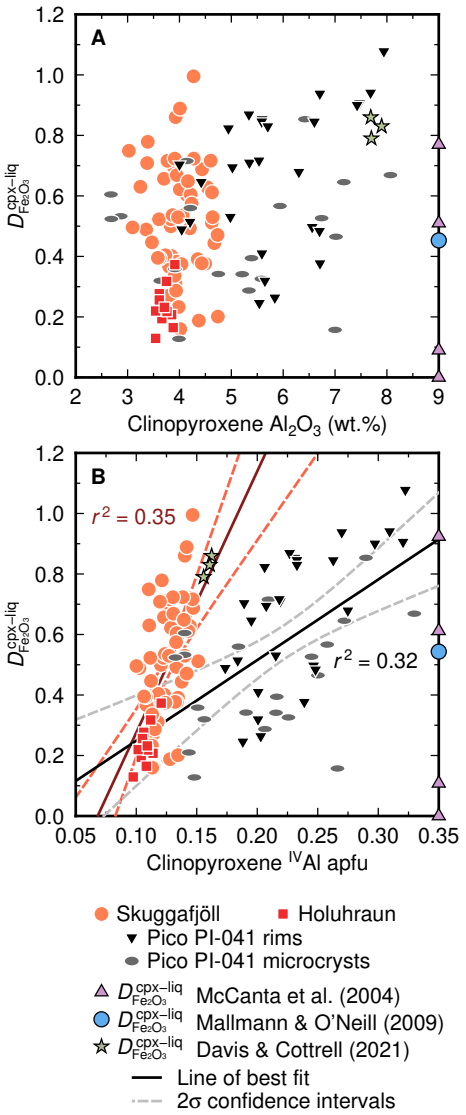

Figure 12: Estimates of $D^{cpx-liq}_{Fe_2O_3}$ from clinopyroxene-liquid pairs in samples from Skuggaföll, Holuhraun and Pico (PI-041) that are textural equilibrium. Clinopyroxene Fe^{3+} contents were determined by stoichiometry following Droop (1987) and liquid (i.e., glass) Fe^{3+} contents were estimated via olivine-liquid equilibria (Figure 11). Published $D^{cpx-liq}_{Fe_2O_3}$ estimates from McCanta et al (2004), Mallmann and O'Neill (2009) and Davis and Cottrell (2021) are shown; compositional information is not available for McCanta et al (2004) or Mallmann and O'Neill (2009). (A) Clinopyroxene Al_2O_3 contents correlate weakly and positively with $D^{cpx-liq}_{Fe_2O_3}$ in our samples, and our estimated $D^{cpx-liq}_{Fe_2O_3}$ values span the same range as published estimates.(B) Clinopyroxene ^{IV}Al contents correlate positively and modestly with $D^{cpx-liq}_{Fe_2O_3}$, consistent with clinopyroxene Fe^{3+} contents being mediated by the abundance of esseneite (Es, $CaFe^{3+}AlSiO_6$) component and implying a strong steric control over Fe^{3+} partitioning.

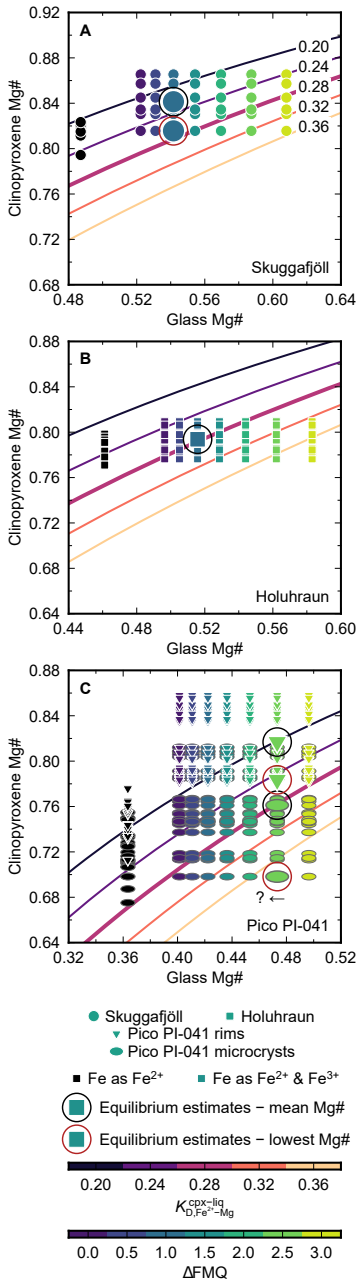

Figure 13: The effect of Fe^{3+} on Fe^{2+}–Mg exchange between clinopyroxene crystals and their host glasses in samples from: (A) Skuggafjöll, Iceland (B) Holuhraun, Iceland, and (C) Pico (PI-041), Azores. Coloured lines show $K^{\mathrm{cpx-liq}}_{\mathrm{D,Fe^{2+}-Mg}}$ values; a nominally equilibrium value of 0.28 determined with Equation 35 of Putirka (2008) at 1200°C is shown with a thicker line; this equation assumes that all Fe is present as Fe^{2+} and thus returns $K^{\mathrm{cpx-liq}}_{\mathrm{D,Fe-Mg}}$ values. Black symbols show clinopyroxene-liquid equilibria calculated assuming that all Fe occurs as Fe^{2+}, as recommended by Wieser et al (2023b). Coloured symbols show values calculated with clinopyroxene Fe^{2+} contents determined by stoichiometry following Droop (1987) and liquid (i.e., glass) Fe^{2+} contents fixed at a range of different oxygen fugacity (f_{O_2}) conditions according to the model of Borisov et al (2018). Large symbols show mean clinopyroxene compositions at f_{O_2} conditions estimated via olivine-liquid equilibria (Figure 11). See the main text for a discussion about whether mean- or lowest-Mg# clinopyroxene compositions provide the best estimate of equilibrium in each clinopyroxene population.

Appendix A Scheme for assigning clinopyroxene components

The following scheme for assigning clinopyroxene components is described in Part I and repeated here for reference:

1. Calculate clinopyroxene cation fractions (X_{cation}) from oxide concentrations on a six oxygen basis
2. Determine clinopyroxene $X_{Fe^{2+}}$ and $X_{Fe^{3+}}$ contents following Droop (1987) encompassing the renormalisation of cations (including total Fe) by multiplying each cation by T/S as outlined in his point (iv); the total number of all original cations will now equal four and values of $X_{Fe^{2+}}$ and $X_{Fe^{3+}}$ can be used to convert FeO_T into FeO and Fe_2O_3
3. Determine the relative proportions of tetrahedral and octahedral Al (^{IV}Al and ^{VI}Al, respectively) such that $X_{^{IV}Al} = 2 - X_{Si}$ and $X_{^{VI}Al} = X_{Al} - X_{^{IV}Al}$; if X_{Si} exceeds 2 there is no $X_{^{IV}Al}$
4. Form Jd ($NaAlSi_2O_6$) from whichever is less between Na and ^{VI}Al such that $X_{Jd} = X_{Na}$ or $X_{Jd} = X_{^{VI}Al}$
5. Form Ae ($NaFe^{3+}Si_2O_6$) from whichever is less between Na remaining after Jd formation and Fe^{3+} such that $X_{Ae} = X_{Na} - X_{Jd}$ or $X_{Ae} = X_{Fe^{3+}}$
6. Form Np($NaFe^{2+}_{0.5}Ti_{0.5}Si_2O_6$) from any Na remaining after Ae formation such that $X_{Np} = X_{Na} - X_{Jd} - X_{Ae}$; only relevant for alkali clinopyroxenes
7. Form Es ($CaFe^{3+}AlSiO_6$) from any Fe^{3+} remaining after Ae formation such that $X_{Es} = X_{Fe^{3+}} - X_{Ae}$
8. Form CaTs ($CaAlAlSiO_6$) from any $X_{^{VI}Al}$ remaining after Jd formation such that $X_{CaTs} = X_{^{VI}Al} - X_{Jd}$
9. Form CaTi ($CaTiAl_2O_6$) from any Ti remaining after Np formation such that $X_{CaTi} = X_{Ti} - X_{Np}/2$; Np is only present in alkali clinopyroxenes
10. Form CrAlTs ($CaCrAlSiO_6$) from Cr such that $X_{CrAlTs} = X_{Cr}$
11. Form DiHd ($Ca(Mg,Fe^{2+},Mn)Si_2O_6$) from any Ca remaining after Es, CaTs, CaTi and CrAlTs formation such that $X_{DiHd} = X_{Ca} - X_{Es} - X_{CaTs} - X_{CaTi} - X_{CrAlTs}$
12. Form EnFs ($(Mg,Fe^{2+},Mn)_2Si_2O_6$) from any Mg, Fe^{2+} and Mn remaining after DiHd formation such that $X_{EnFs} = (X_{Mg} + X_{Fe^{2+}} + X_{Mn}) - X_{DiHd}/2$